

# Final Report

## Cover Page

**Report Number:** DOE-PBL-21578

**DOE Award Number:** DE-SC0021578

**Sponsoring Program Office:** DOE Office of Science

**Name and Address of Recipient:** Particle Beam Lasers, Inc.  
8800 Melissa Court  
Waxahachie, TX 75167-7279

**Project Title:** A new medium field superconducting magnet for the EIC

**Principal Investigator:** Ramesh Gupta

**Team Members BNL:** Kathleen Amm, Michael Anerella, Jason Becker, Raymond Ceruti,  
John Escallier, Ramesh Gupta, Piyush Joshi, Andrew Marone,  
Brett Parker, Thomas Van Winckel, Anis Ben Yahia

**Team Members PBL:** Stephen Kahn, James Kolonko, Delbert Larson, Ronald Scanlan,  
Robert J. Weggel, Erich Willen, Albert Zeller

**Acknowledgement:** This material is based upon work supported by the U.S. Department of Energy, Office of Science, Office of Nuclear Physics, under Award Number DE-SC0021578.

**Disclaimer:** This work was prepared as an account of work sponsored by an agency of the United States Government. Neither the United States Government nor any agency thereof, nor any of their employees, makes any warranty, express or implied, or assumes any legal liability or responsibility for the accuracy, completeness, or usefulness of any information, apparatus, product, or process disclosed, or represents that its use would not infringe privately owned rights. Reference herein to any specific commercial product, process, or service by trade name, trademark, manufacturer, or otherwise, does not necessarily constitute or imply its endorsement, recommendation, or favoring by the United States Government or any agency thereof. The views and opinions of authors expressed herein do not necessarily state or reflect those of the United States Government or any agency thereof.

### **20 YEAR SBIR/STTR DATA RIGHTS (2019)**

**Funding Agreement No:** DE-SC0021578

**Award Date:** 03/03/2021

**SBIR/STTR Protection Period:** Twenty years from Award Date

**SBIR/STTR Awardee:** Particle Beam Lasers, Inc.

This report contains SBIR/STTR Data to which the Federal Government has received SBIR/STTR Technical Data Rights or SBIR/STTR Computer Software Rights during the SBIR/STTR Protection Period and Unlimited Rights afterwards, as defined in the Funding Agreement. Any reproductions of SBIR/STTR Data must include this legend.

**Project Summary / Abstract**

**Company Name and Address:** Particle Beam Lasers, Inc.  
8800 Melissa Court  
Waxahachie, TX 75167-7279

**Principal Investigator:** Ramesh Gupta

**Project Title:** A new medium field superconducting magnet for the EIC

**Purpose of Research, Research Carried Out, and Research Findings:**

Most superconducting accelerator magnets are presently based on a conventional *cosine theta* design. Typically, the magnet's length is much greater than its diameter, and the loss in effective length from the ends (about a coil diameter in typical dipoles) is relatively small. However, for relatively short magnets such as those envisioned for the Interaction Region (IR) of the Electron Ion Collider (EIC), the end effects of the conventional design will result in a relatively large reduction of the integrated field.

This proposal is for developing a *direct wind* magnet based on the *optimum integral design* wherein we will use robotics to lay down the magnet wires as directed by a computer, allowing for extremely efficient and optimized placement of every portion of the wires. This promises to reduce loss of effective length due to the ends, with the effective length approaching the coil length. In the *optimum integral design* approach, the ends become an integral part of the magnet body, thereby creating a higher integral field for the same coil length, which also increases the operating margin. The more compact design is critical when the available space is limited as in the EIC.

During Phase I, we ported and developed computer codes for further optimizing the *optimum integral design*. The lower cost of building magnets with the *direct wind* technology allowed us to design, build, and demonstrate a 2-layer, 1.7 T, 600 mm long superconducting dipole in Phase I. We also developed initial magnetic and mechanical designs of the dipole to be constructed and tested in Phase II.

During Phase II, we will further optimize the design and build the magnet. Once built, we will perform quench tests and field quality measurements on the magnet. Finally, we will examine the applicability of the *optimum integral design* to other EIC magnets and for other applications such as medical and accelerator beamlines where compact, medium field superconducting magnets are required.

**Potential Applications of the Research:**

A *direct wind* magnet based on the *optimum integral design* will create higher quality fields and have lower adverse end effects than conventional designs making it ideal for uses wherein space is at a premium. Demonstration of the *direct wind* magnet based on the *optimum integral design* is expected to provide a superior technical solution and reduce the cost of developing and building such magnets. These magnets should find widespread use in particle accelerators for research and medical applications.

# CONTENTS

|   |    |
|---|----|
| Contents.....   | 3  |
| 1 Introduction.....   | 4  |
| 1.1 Background Information .....  | 4  |
| 1.2 Identification and Significance of the Problem .....                                    | 4  |
| 1.2.1 Direct Wind Technology .....  | 5  |
| 1.2.2 Coil End Designs.....   | 6  |
| 1.2.3 EIC Interaction Region B0APF Dipole.....  | 7  |
| 1.3 Technical Approach.....   | 8  |
| 2 Technical Objectives .....  | 9  |
| 2.1 Optimum Integral Design of EIC IR Dipole B0APF.....                                     | 9  |
| 2.2 Proof-of-Principle Optimum Integral Design for B0APF .....                              | 9  |
| 2.3 4 K Test of the Proof-of-Principle Optimum Integral Dipole .....                        | 10 |
| 3 Significant Achievements During Phase I for a Strong Phase II Proposal .....              | 10 |
| 3.1 Software upgrades to optimize the design .....  | 11 |
| 3.2 Selection of the conductor .....  | 14 |
| 3.3 Design optimization of the proof-of-principle dipole.....                               | 14 |
| 3.4 Winding of the proof-of-principle optimum integral dipole coil.....                     | 16 |
| 3.5 Preparation of the proof-of-principle dipole for a 4 K test.....                        | 22 |
| 3.6 Proof-of-principle dipole test at 4 K.....  | 22 |
| 3.7 Comparison Between calculations and measurements in the Proof-of-principle dipole ..... | 23 |
| 3.8 Magnetic, mechanical and winding optimization for the Phase II magnet.....              | 24 |
| 3.8.1 Magnetic Design and Analysis .....  | 24 |
| 3.8.2 Mechanical Analysis with COMSOL.....  | 26 |
| 3.8.3 Mechanical Analysis with ANSYS .....  | 28 |
| 4 SUMMARY .....   | 42 |
| 5 References.....   | 43 |

# 1 INTRODUCTION

## 1.1 BACKGROUND INFORMATION

Following the recommendation of the Nuclear Science Advisory Committee (NSAC) [1] and of the Long Range Plan (LRP) for Nuclear Science [2] to make the proposed Electron Ion Collider (EIC) the highest priority for new construction, the Department of Energy (DoE) is now proceeding with the next phase of pursuing the EIC. The EIC will be the next major research facility in the United States, and it is expected to answer several basic questions such as “where does the proton mass come from?” Through its collisions, the EIC will also deepen our understanding of the internal structure of ordinary matter via the interactions of its elementary constituents, the quarks, and gluons. By providing this better understanding, the EIC is expected to help us unlock the secrets of the strongest force in nature. Beyond sparking scientific discoveries, building the EIC is also expected to trigger broader benefits for society. The estimated cost of the proposed Electron Ion Collider is \$1.6 billion to \$2.6 billion [3]. The EIC will be built at the Brookhaven National Laboratory (BNL) [4] with active participation of the Thomas Jefferson National Accelerator Facility (TJNAF) [5].

The EIC will consist of two intersecting accelerators, one producing an intense beam of electrons, the other a high-energy beam of protons or heavier atomic nuclei. These two beams will then be steered into head-on collisions. Fig. 1 shows the layout of the entire complex, including the collider, other accelerators and the ion sources [6]. Whereas the electron ring will be a new ring constructed with new magnets and other hardware, the proton ring will use many of the existing superconducting magnets from the presently operating Relativistic Heavy Ion Collider (RHIC). The Interaction Region (IR) between the electron and ion beams will primarily consist of new hardware, including new detectors and new magnets.

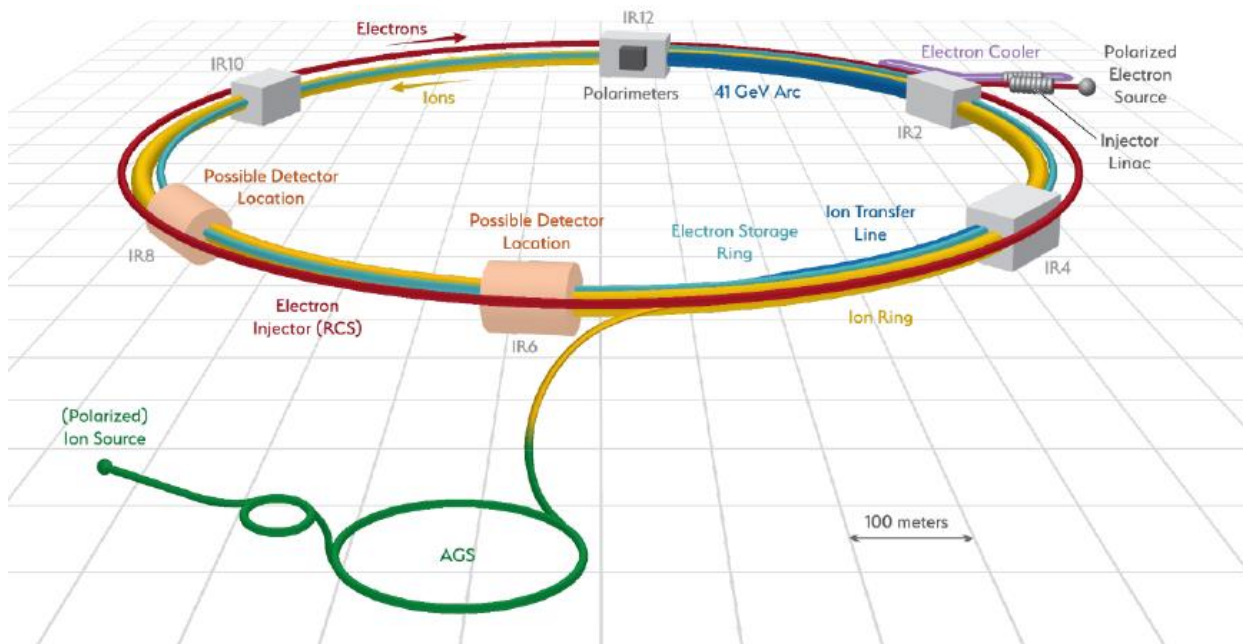


Figure 1: Layout of the proposed Electron Ion Collider (EIC).

## 1.2 IDENTIFICATION AND SIGNIFICANCE OF THE PROBLEM

This report addresses the superconducting magnets in the Interaction Region (IR) of the EIC. Superconducting magnets are used only for the hadron (proton or ion) beams which require much higher magnetic fields than does the electron beam. (Room temperature copper-coil-based magnets will suffice for the electron beam because of the lower field requirements.) The current layout [6] of the EIC IR is shown in Fig. 2. The figure on the left shows the beamlines and important components both upstream (rear) and downstream (forward) from the ion beam perspective. The figure

on the right shows the forward side. The basic parameters of the forward side magnets for the hadron beam are given in Table 1.

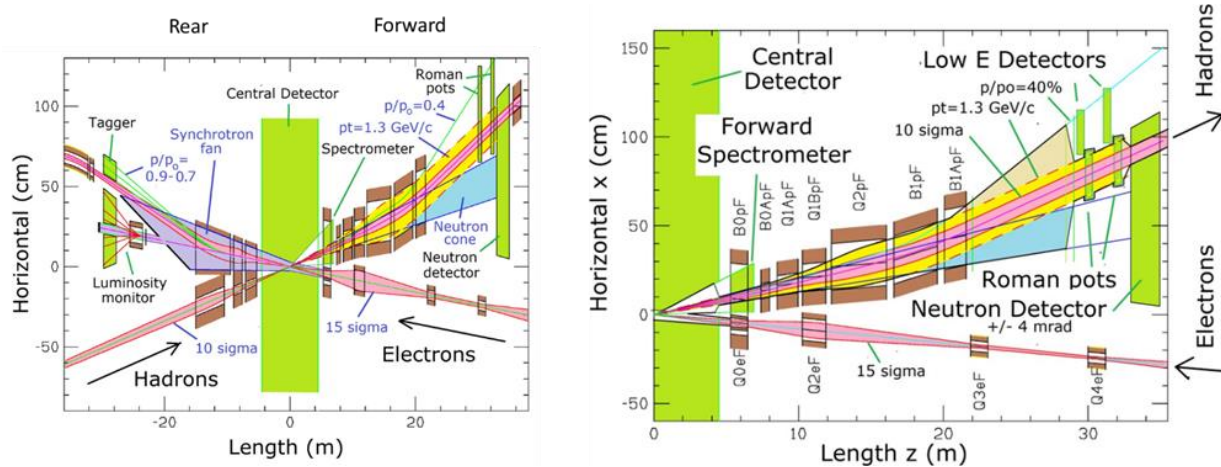


Figure 2: Schematic layout of the EIC interaction region (top view). The figure on the left shows the hadron and electron beamlines on both sides of the central detector. The figure on the right shows more details of the hadron-downstream-side (the ‘forward’ side). The above figures incorporate the dipole and quadrupole magnets for both beams (electron and hadron), spectrometer magnets, and other major components of the IR.

Table 1: Forward hadron magnets for 275 GeV operation

| FORWARD DIRECTION                     | Hadron Magnets |       |         |        |        |        |        |
|---------------------------------------|----------------|-------|---------|--------|--------|--------|--------|
|                                       | B0PF           | B0APF | Q1APF   | Q1BPF  | Q2PF   | B1PF   | B1APF  |
| Center position [m]                   | 5.9            | 7.7   | 9.23    | 11.065 | 14.170 | 18.070 | 20.820 |
| Length [m]                            | 1.2            | 0.6   | 1.46    | 1.6    | 3.8    | 3.0    | 1.5    |
| Center position w.r.t. to x-axis [mm] | -15            | 55    | 140     | 238    | 407    | 390    | 800    |
| Angle w.r.t. to z-axis [mrad]         | -25.0          | 0.0   | -5.5    | -10.0  | -10.2  | 9.0    | 0.0    |
| Beam tube radius [mm]                 | 200            | 43    | 56      | 78     | 131    | 135    | 168    |
| Coil inner diameter [mm]              | ---            | 120   | 142     | 186    | 330    | 300    | 370    |
| Peak field [T]                        | -1.3           | -3.3  | 0.0     | 0.0    | 0.0    | -3.4   | -2.7   |
| Gradient [T/m]                        | 0.0            | 0.0   | -72.608 | -66.18 | 40.737 | 0.0    | 0.0    |

The magnets listed in Table 1 are superconducting magnets and only one of each is needed. In such cases the cost of engineering design and analysis together with the cost of various tooling becomes a significant factor in determining the cost of each magnet. To minimize such cost several magnets are being proposed to be built using “Direct Wind Technology” (see section 1.2.1).

Another noteworthy aspect of the magnets shown in Table 1 is the ratio of the coil length (given in meters) to the coil aperture (given in mm). This ratio in most superconducting magnets is well over an order of magnitude, but this is not the case for some EIC magnets, such as the dipole B0APF. This means that the ends will play a significant role in the magnet by increasing the required field in the body of the magnet (see section 1.2.2).

### 1.2.1 Direct Wind Technology

Direct Wind Technology [7] is a process where superconducting wire or small diameter round cable is directly bonded on an insulated beam tube coated with b-stage epoxy. The bonding is created with local heating created with ultrasound, followed by rapid cooling. The wiring pattern is laid on the tube via a computer-controlled multi-axis winding machine with a winding head supported in a gantry which traverses along the length of the tube while the tube rotates on its axis. After the winding is completed, small gaps between conductors are filled with a matching thermal expansion epoxy or pieces of other custom-cut insulator (such as Nomax®), depending on the size of the gap. The coil

is then wrapped with multiple layers of tensioned fiberglass roving, epoxied and cured. The amount of tension to be provided by the fiberglass depends on the amount of pre-stress needed on the coil. These steps make a package that can withstand a significant amount of Lorentz forces as has been demonstrated in the “Direct Wind” magnets made so far. If needed for future magnets with higher field and larger aperture, this structure can be placed in a stainless steel or high strength Aluminum tube which will provide an additional support.

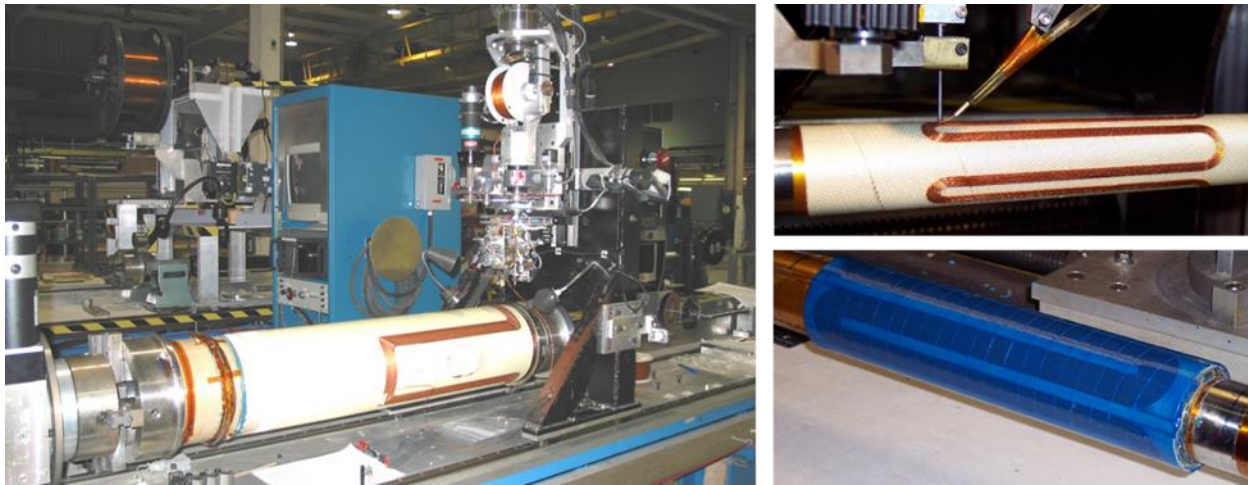


*Figure 3: The Direct Wind Machine with its main components (left); superconducting wire directly being laid on the insulated tube and bonded with ultrasound heating (top-right); and final package after filler/epoxy addition (bottom-right).*

The winding pattern and gaps determine the type of magnet (dipole, quadrupole, sextupole, octupole, etc.) and field quality. These are pre-computed via a separate computer program for each layer. In fact, by measuring the field quality in between the layers, subsequent layers can correct the residual errors of the previous layer and thus create a highly accurate magnetic field. Earlier magnets of this type with lower self-field or smaller aperture than the EIC magnets have reached the short sample field with almost no quenches.

A similar technology is being used at the Advanced Magnet Lab [8].

The major cost and schedule benefit of the direct wind technology is that it avoids the need for detailed engineering as well as the cost of various tooling and support structures that are required for conventional superconducting magnets made with Rutherford cable. These up-front costs are relatively small if the number of magnets based on each design is large but becomes a major portion of budget and schedule for single magnet production. Therefore, extending and demonstrating the “Direct Wind” technology to the higher fields and larger apertures required for many EIC magnets will provide major cost and schedule savings and retire significant risk. The demonstration of a design that helps achieve this task could be a game changer, not only for the EIC, but for similar applications in the future.

### 1.2.2 Coil End Designs

A magnet coil is described by two parts: (a) the ‘body’ portion of the magnet where the coil pattern remains similar as the conductor in each turn moves along the length and b) the two ‘end’ portions on either side of the coil where the winding wraps from one side to the other so that the direction of current can be changed. In most magnets the length of the body of the magnet is over an order of magnitude greater than an individual end. In cosine theta dipoles, the length of each end is 1.5 to 2 times the coil diameter as shown in Fig. 4 (left) [9]. For the RHIC arc dipoles made with Rutherford cable a similar ratio is seen in “Direct Wind” magnets as well. Moreover, the average field in the end sections is smaller than the field in the same length of the straight section. The integral field is about 2/3 (or even less in many cases) of that for the same length of straight section. The effective magnetic length, defined as the field integrated over the length of the magnet divided by the body field, is therefore smaller than the coil length. The typical loss in the effective magnetic length over the coil length due to ends in cosine theta magnets is of the order of a coil diameter for dipoles, a coil radius for quadrupoles, etc.

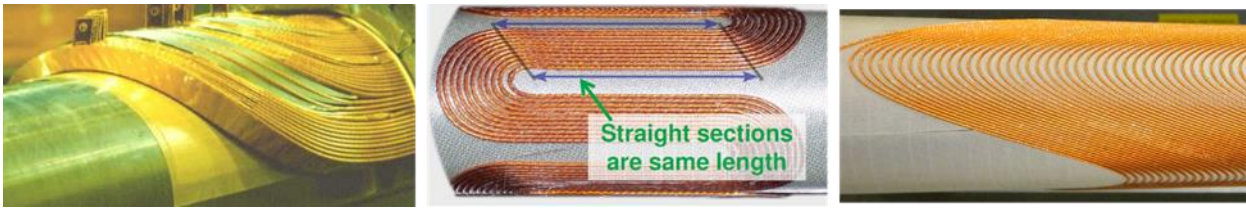


Figure 4: (a) Ends of the cosine theta design (left); (b) Straight section and ends of the serpentine design (middle); and (c) End region of the first layer of the double helix design (right).

The *Serpentine* design [10] is being used in most “direct wind” magnets at BNL as it offers several advantages. In the Serpentine design (see Fig. 4 center), a coil of any number of poles is continuously wound with the end-turns for each layer of turns located only on one end azimuthally, with the return end being located in the next azimuthal turn. Since each turn is successively moved axially by a similar ( $\sim$ wire diameter) length, the length of every turn remains the same. In the limiting case where the bend radius of each turn in the end approaches zero, the integral field and the field harmonics in the entire coil will be the same as those in the 2D section, even when no end-spacers are used. Therefore, to a good approximation, the integral field will be given by the “2D field” multiplied by the “coil length minus the space taken by the end turns”. Therefore, the loss in effective magnetic length is still about a coil diameter for dipoles and a coil radius for quadrupoles.

The third geometry used for Direct wind magnets is the Double helix coil. This geometry has been used recently at BNL for the “tapered quad” [11] and at Advanced Magnet Lab [8] for various magnets. Fig. 4 (right) shows the end region of the first layer of the double helix design. Note that the end span of the second layer will be cutting halfway through the end span of the first layer. The loss in the magnetic length of the double helix design remains at least as much as in the other designs and is often even more.

### 1.2.3 EIC Interaction Region B0APF Dipole

B0APF is a 120 mm coil aperture dipole in the Interaction Region of the proposed electron ion collider. A 3.3 T bore field requirement makes it a relatively high field dipole for the direct wind technology at such a large aperture. The current design is based on Rutherford cable. Major parameters of the B0APF dipole are given in Table 2 and the superconducting coil with field contour superimposed over the coil body and coil ends is shown in Fig. 5. The allocated space for the superconducting coils of this magnet is only about five times the coil aperture. As mentioned earlier, coil ends typically reduce the effective magnetic length of the dipole by about a coil aperture. In the case of the B0APF dipole this is a significant loss (approximately 20%). To compensate for this loss the field in the body would have to be increased, which is a significant penalty.

Table 2: Parameters of the B0APF magnet

| Parameter                            | Value                            |
|--------------------------------------|----------------------------------|
| Maximum dipole field [T]             | 3.3                              |
| Coil Aperture [mm]                   | 120                              |
| Magnet Bore [mm]                     | 90                               |
| Required field quality               | $1 \times 10^{-4}$               |
| Physical length [m]                  | 0.6                              |
| Physical width [m]                   | 0.16                             |
| Physical height [m]                  | 0.16                             |
| Superconductor type                  | NbTi                             |
| Conductor [mm <sup>2</sup> ]         | RHIC cable, 9.73 $\times$ 1.2679 |
| Current density [A/mm <sup>2</sup> ] | 421                              |
| Cu:Sc ratio                          | 2                                |
| Temperature [K]                      | 4.2                              |
| Peak field wire [T]                  | 4.36                             |
| Magnetic energy [J]                  | 264000                           |
| Ampere turns [A-t]                   | 343200                           |
| Number of turns                      | 78                               |
| Current [A]                          | 4400                             |
| Inductance [H]                       | 0.027273                         |
| Margin loadline [%]                  | 30                               |

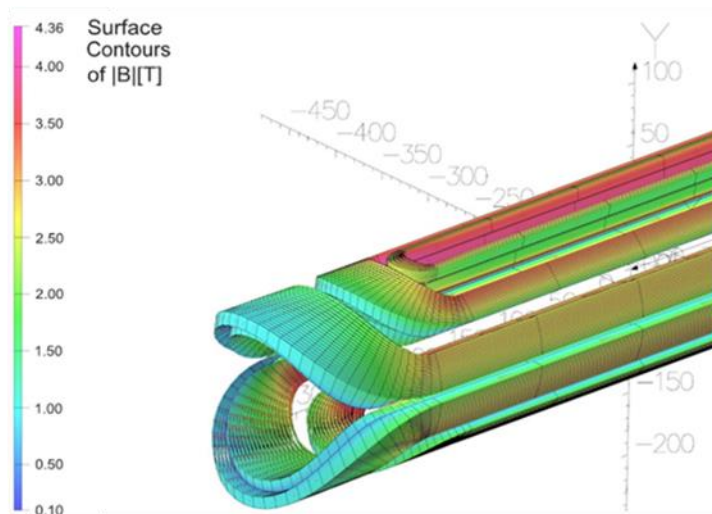


Figure 5: B0APF coil with field contour superimposed on the body and ends.



## 2 TECHNICAL OBJECTIVES

The three main technical objectives of Phase I were (a) development of an optimum integral design with direct wind technology of a medium field, large aperture magnet with the EIC IR dipole B0APF as the specific example, (b) development of a scaled down proof-of-principle magnet that can be built in the budget of Phase I, and (c) demonstration of the proof-of-principle magnet with a 4 K test. This was an ambitious plan for the budget and schedule limits of a Phase I proposal; however, we were hopeful that it could be achieved thanks to the benefit of the direct wind approach, as mentioned in the last section.

### 2.1 OPTIMUM INTEGRAL DESIGN OF EIC IR DIPOLE B0APF

The first objective of Phase I was to develop an optimum integral design with direct wind technology of a medium field, large aperture dipole with EIC IR dipole B0APF as the example. The initial concept of the design as presented in the Phase I proposal is shown in Fig. 7. Fig 7(a) shows the magnetic field superimposed on the coil and on the upper half of the yoke. Fig. 7(b) shows midplane turns in the ends of the optimum integral design extending the full coil length (except for a small bend radius) to increase the effective length. Fig 7(c) shows the vertical component of the field on the axis.

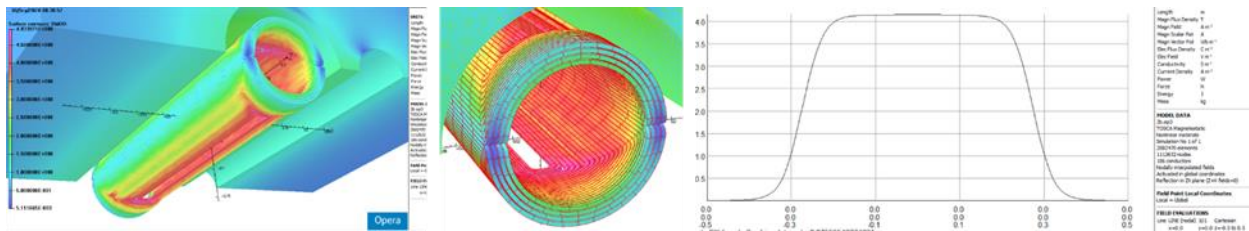


Figure 7: (a) Coil and upper half of the yoke with field superimposed; (b) Ends of the optimum integral design with the midplane turns extending to nearly the full coil length; and (c) Vertical component of the field along the axis.

It was earlier shown that the optimum integral design can produce good field quality even in short dipoles [12]. The technical objective of Phase I was to develop a good field quality design for B0APF. The number and size of spacers in the body and in the ends would be used as parameters to optimize the field quality and to reduce the peak fields both in the body and in the ends of the magnet. Fig. 8 and Table 3 shows the results of an earlier optimization for a dipole with a coil diameter of 200 mm and a length of  $\sim 175$  mm (coil length less than a coil diameter). The goal of Phase I was to optimize such a design for B0APF.

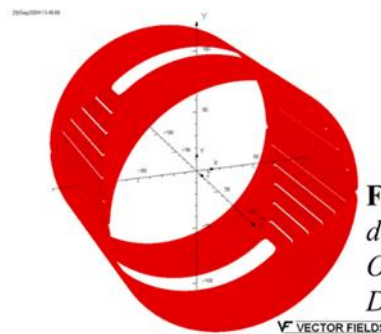


Figure 8: A short dipole based on the Optimum Integral Design.

Table 3: Computed Integral Field Harmonics for a Short Dipole (coil length < diameter) at a Radius of 66.6 mm. The Coil Radius is 100 mm. Note  $b_2$  is sextupole multiplied by  $10^4$  (US conventions).

| $b_2$ | $b_4$ | $b_6$ | $b_8$ | $b_{10}$ | $b_{12}$ |
|-------|-------|-------|-------|----------|----------|
| 0.0   | 0.0   | 0.0   | 0.0   | 0.0      | 0.0      |

The support structure will have intermediate stainless-steel tube(s) to intercept the Lorentz forces, along with the pre-tensioned fiberglass wrap that has been always placed over the direct-wind coils.

### 2.2 PROOF-OF-PRINCIPLE OPTIMUM INTEGRAL DESIGN FOR B0APF

Another technical objective of Phase I was to develop the design of a proof-of-principle optimum integral dipole that will achieve nearly the highest possible integral field at a reasonable length that can be built and tested within the budget of Phase I. As the next section will describe, we achieved significantly more than the goals outlined in the

proposal for the latest parameters of the design. The goals, as mentioned in Phase I proposals were: 1) it will be a 2-layer design; 2) it will have the same coil diameter as that of B0APF (120 mm); 3) it will have as many turns as possible to maximize the field while having a typical pole; and 4) it will have representative spacers both in the body and in the ends of the magnet. The coil will have a length of 150 mm, as compared to the 500 mm specified for B0APF.

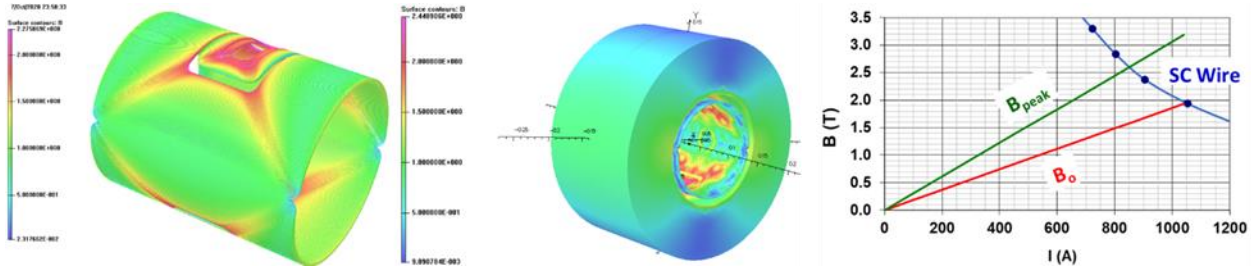


Figure 9: (a) Initial 2-layer coil design of the proof-of-principle optimum integral dipole design with the field contour superimposed on the coil at 800 A; (b) Initial design with additional field from the iron yoke; and (c) Load line for the peak field and field at the center of the dipole with an expected short sample current of 850 A.

The design, as mentioned in the Phase I proposal, is shown in Fig. 9. It was based on the 1 mm diameter cable which was in stock (surplus from a previous project). A maximum field of 2.6 T on the superconductor and 1.6 T in the bore of the magnet was expected at 850 Amperes based on the computed short sample of the conductor that was available.

### 2.3 4 K TEST OF THE PROOF-OF-PRINCIPLE OPTIMUM INTEGRAL DIPOLE

The major technical objective and the highlight of Phase I was the construction and quench test of the proof-of-principle optimum integral dipole design. A successful outcome and experience of this would put the Phase II proposal on a strong footing. The initial design was iterated, the superconducting coil was wound on the BNL direct wind machine, and the magnet was tested in the iron yoke at  $\sim 4.2$  K to the quench field.

## 3 SIGNIFICANT ACHIEVEMENTS DURING PHASE I FOR A STRONG PHASE II PROPOSAL

The technical objective outline, in the previous section, was ambitious for the budget and schedule of a Phase I. To achieve them, the Phase I Work Plan was divided into several specific tasks with each task monitored very carefully while looking for opportunities to do more where possible or found necessary. One such opportunity involved the length of proof-of-principle magnet. While carrying out a more detailed design of B0ApF for Phase II (which is 600 mm long) and comparing it with the one mentioned in the Phase I proposal (which is 150 mm long), major technical differences were observed. Therefore, the length of Phase I proof-of-principle magnet was changed to 600 mm. The additional cost of conductor didn't play a role since spare conductor was used at no cost to this project and the labor associated with the increased length was minimal. Making the Phase I coils similar in length to the proposed Phase II inner coils not only makes them more representative to the final magnet, but also allows the coils wound and tested in Phase I to be utilized in Phase II.

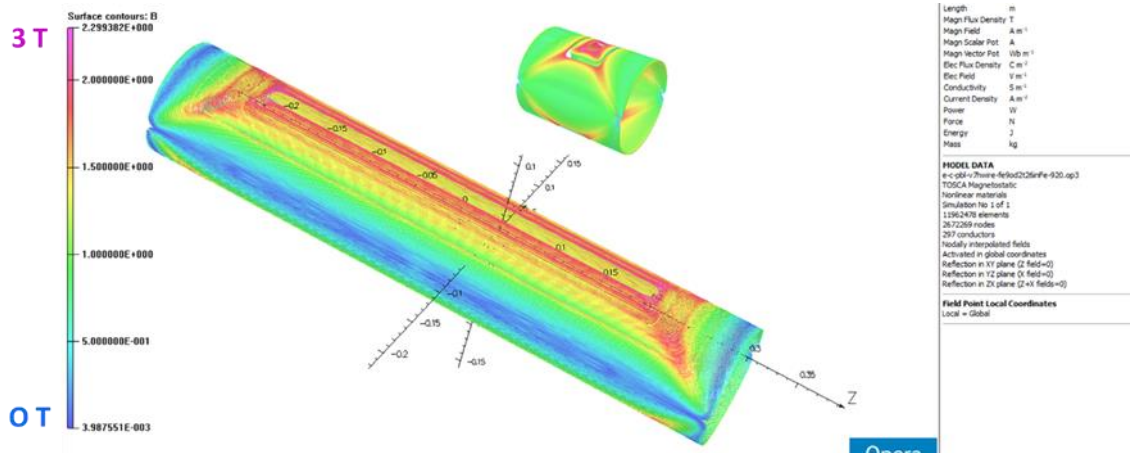


Figure 10: Models of two coils with field superimposed (a) 150 mm long 2-layer coil design as mentioned in the Phase I proposal; (b) 600 mm long design of the inner-most 2-layer coil of the BOApF dipole as investigated for Phase II. Because of the major technical differences between the two coils, a shorter 150 mm long coil would not have been a good representation for the magnet to be built in Phase II and therefore the coil length of the Phase I coil was increased to 600 mm.

Measurements on the field along the length of magnet (not listed as a task in the Phase I proposal) could be performed at room temperature to test the key touted benefit of the optimum integral design for extending the effective length of the magnet. Measurements were compared against the calculations.

The list of technical tasks from Phase I proposal is used below to summarize the significant achievements made during Phase I.

### 3.1 SOFTWARE UPGRADES TO OPTIMIZE THE DESIGN

The software to do initial optimization of the optimum integral design was developed primarily on a VAX/VMS computer and ported to a PC over a decade ago using a DEC FORTRAN compiler. It also uses several CERN software libraries [13] to optimize the design. The software was partly ported to CYGWIN [14] to initialize optimization. The first task of this proposal was to fully port this software to CYGWIN and a LINUX platform. The software was upgraded to include more features for optimization. These included different turn-to-turn spacing between the ends and body of the magnet. These were required for laying out the turns more robustly while using the direct wind technology and provides an additional feature in optimizing the field harmonics. A new feature was added where the turn-to-turn spacing could be changed between the blocks of conductor of the same layer both in the body and end of the magnet. These are features which are easy to implement in a coil wound with direct wind technology and plays a significant role in reducing the peak-fields on the conductor, as well as reducing the field harmonics. Finally output functions to create an OPERA3D file and for direct wind software were enhanced. While preparing a user manual will be part of the Phase II proposal, example files are given below.

An example of input file \*.X01:

```

$FCNX VC2CB=.TRUE.,VC2CE=.TRUE.,MAGTYPE=2,LAYERS=1,RFEMM=110,R0MM=40.,
      RBENDMM=10,NBEND=10,ENDCONFIG=1,TAPER=.TRUE.,TAPERTYPE=0, &end
2 2 0.3 3. 100. 800 2. 0.1 50. 100
B2 0. 1.
B4 0. 1.
    
```

An example of input file \*.X07:

```

2 BODY & 2 ENDS, 1 LAYER, (CONSTANT VC2CB & VC2CE)
1 W1      1.      0.      0.      19.
2 N1      15.     0.      20.     42.
3 B1      0.      0.      0.      9.
4 W2      6.      0.1     1.      9.5
5 N2      5.      0.      10.     20.
6 B2      0.1     0.01   0.      0.2
10 S1     0       0.      0.      20.
11 T1     10.     0.      4.      29.
12 E1     0.      0.0    0.      10.
13 S2     50.     0.1    0.      100.
14 T2     10.     0.      0.      29.
15 E2     9.      0.1    0.      50.0
          0.0
CALL FCN      3.
CALL FCN      3.  1.
END RETURN
    
```

An example of partial output file \*.X11:

```

Turn-to-turn insulation ends(mm)  0.400000006
Turn-to-turn insulation body(mm)  0.200000003
CURRENT PER WIRE (AMP)           500.000000
NUMBER OF CROSS SECTION BLOCKS AND No. OF END BLOCKS
          2          2
REFERENCE PARAMETERS BY COUNTING FROM MIDPLANE
LAYER NO.  BLOCK NO.  TURN NO.  WEDGE (DEGREE)  C2C-BODY (DEG)
1          1          48      0.00000          0.00000
1          2          15      1.57930          0.18000
1          3           5      1.00000          0.51000
LAYER NO.  BLOCK NO.  TURN NO.  END-SPACER (MM)  C2C-END (MM)
1          1          48      0.00000          0.00000
1          2          15      1.95200          0.18500
1          3           5      5.00000          0.49500
LAYER NO.  BLOCK NO.  TURN NO.  WEDGE (DEGREE)  C2C-BODY (DEG)
2          1          35      0.00000          0.00000
2          2          19      2.36100          0.14100
2          3           6      4.71490          0.99800
LAYER NO.  BLOCK NO.  TURN NO.  END-SPACER (MM)  C2C-END (MM)
2          1          35      0.00000          0.00000
2          2          19      0.03600          0.05300
2          3           6      5.03420          0.22300
LAYER NO.  BLOCK NO.  TURN NO.  WEDGE (DEGREE)  C2C-BODY (DEG)
3          1          51      0.00000          0.00000
3          2          18      8.17380          0.20000
LAYER NO.  BLOCK NO.  TURN NO.  END-SPACER (MM)  C2C-END (MM)
3          1          51      0.00000          0.00000
3          2          18      0.12545          0.00700
LAYER NO.  BLOCK NO.  TURN NO.  WEDGE (DEGREE)  C2C-BODY (DEG)
4          1          62      0.00000          0.00000
4          2           9      2.23010          0.10000
LAYER NO.  BLOCK NO.  TURN NO.  END-SPACER (MM)  C2C-END (MM)
4          1          62      0.00000          0.00000
4          2           9      0.00000          0.01200
CHI SQUARE = 6.3857675269246101
INTEGRATED FIELD HARMONICS :
No.  Bn(T.m)  bn*10^4(units)  bn(des)  weight
0  0.82536E+00  10000.0000  0.0000  0.0000
2  0.14947E-03  1.8109  0.0000  1.0000
4  0.11305E-04  0.1370  0.0000  2.0000
6  0.28539E-04  0.3458  0.0000  5.0000
    
```

An example of partial output file \*.X31:

| LAYER | TURN | RADIUS (MM) | ANGLE (DEG) | TURN-LENGTH (M) | X (MM) | Y (MM) |
|-------|------|-------------|-------------|-----------------|--------|--------|
| 1     | 1    | 73.513      | 0.50327     | 0.600000        | 73.997 | 0.650  |
| 1     | 2    | 73.513      | 1.50982     | 0.597000        | 73.974 | 1.950  |
| 1     | 3    | 73.513      | 2.51637     | 0.594000        | 73.929 | 3.249  |
| 1     | 4    | 73.513      | 3.52292     | 0.591000        | 73.860 | 4.547  |
| 1     | 5    | 73.513      | 4.52946     | 0.588000        | 73.769 | 5.844  |
| 1     | 6    | 73.513      | 5.53601     | 0.585000        | 73.655 | 7.139  |
| 1     | 7    | 73.513      | 6.54256     | 0.582000        | 73.518 | 8.432  |
| 1     | 8    | 73.513      | 7.54911     | 0.579000        | 73.359 | 9.722  |
| 1     | 9    | 73.513      | 8.55565     | 0.576000        | 73.177 | 11.009 |
| 1     | 10   | 73.513      | 9.56220     | 0.573000        | 72.972 | 12.293 |
| 1     | 11   | 73.513      | 10.56875    | 0.570000        | 72.745 | 13.573 |
| 1     | 12   | 73.513      | 11.57530    | 0.567000        | 72.495 | 14.849 |
| 1     | 13   | 73.513      | 12.58184    | 0.564000        | 72.223 | 16.120 |
| 1     | 14   | 73.513      | 13.58839    | 0.561000        | 71.929 | 17.386 |
| 1     | 15   | 73.513      | 14.59494    | 0.558000        | 71.612 | 18.647 |
| 1     | 16   | 73.513      | 15.60149    | 0.555000        | 71.274 | 19.902 |
| 1     | 17   | 73.513      | 16.60803    | 0.552000        | 70.913 | 21.151 |
| 1     | 18   | 73.513      | 17.61458    | 0.549000        | 70.530 | 22.393 |
| 1     | 19   | 73.513      | 18.62113    | 0.546000        | 70.126 | 23.629 |
| 1     | 20   | 73.513      | 19.62767    | 0.543000        | 69.700 | 24.857 |
| 1     | 21   | 73.513      | 20.63422    | 0.540000        | 69.253 | 26.078 |
| 1     | 22   | 73.513      | 21.64077    | 0.537000        | 68.784 | 27.290 |
| 1     | 23   | 73.513      | 22.64732    | 0.534000        | 68.294 | 28.494 |
| 1     | 24   | 73.513      | 23.65387    | 0.531000        | 67.783 | 29.690 |
| 1     | 25   | 73.513      | 24.66041    | 0.528000        | 67.251 | 30.876 |
| 1     | 26   | 73.513      | 25.66696    | 0.525000        | 66.698 | 32.052 |
| 1     | 27   | 73.513      | 26.67351    | 0.522000        | 66.125 | 33.219 |
| 1     | 28   | 73.513      | 27.68005    | 0.519000        | 65.531 | 34.376 |
| 1     | 29   | 73.513      | 28.68660    | 0.516000        | 64.917 | 35.521 |
| 1     | 30   | 73.513      | 29.69315    | 0.513000        | 64.283 | 36.656 |
| 1     | 31   | 73.513      | 30.69970    | 0.510000        | 63.629 | 37.780 |
| 1     | 32   | 73.513      | 31.70624    | 0.507000        | 62.956 | 38.892 |
| 1     | 33   | 73.513      | 32.71279    | 0.504000        | 62.263 | 39.992 |
| 1     | 34   | 73.513      | 33.71934    | 0.501000        | 61.551 | 41.079 |
| 1     | 35   | 73.513      | 34.72589    | 0.498000        | 60.820 | 42.154 |
| 1     | 36   | 73.513      | 35.73243    | 0.495000        | 60.070 | 43.216 |
| 1     | 37   | 73.513      | 36.73898    | 0.492000        | 59.301 | 44.265 |
| 1     | 38   | 73.513      | 37.74553    | 0.489000        | 58.515 | 45.300 |
| 1     | 39   | 73.513      | 38.75207    | 0.486000        | 57.710 | 46.320 |
| 1     | 40   | 73.513      | 39.75862    | 0.483000        | 56.887 | 47.327 |

An example of a partial output \*.cond file:

```

CONDUCTOR
DEFINE GSTR
0.0000000 0.0000000 0.0000000 0.0000000 0.0000000 0.0000000
0.0739971 0.0006500 0.0000000
0.0000000 0.5032737 0.0000000
0.0009748 0.0009748
0.2900000
526132064.00000 -2 10001
-1 0 1
1.0000000
DEFINE GARC
0.0000000 0.0000000 0.0000000 171.7540588 0.0000000 0.0000000
-0.0740000 0.0000000 0.3000000
90.0000000 90.0000000 180.0000000
0.0009748 0.0009748
0.0735126 163.5081024
526132064.00000 -2 20001
-1 0 0
1.0000000
DEFINE BR20
0.0 0.0 0.0 0.0 0.0 0.0
0.0 0.0 0.0
0.0 0.0 0.0
0.073505 0.001133 0.290000
0.073514 0.000158 0.290000
0.074489 0.000167 0.290000
0.074480 0.001142 0.290000
0.072753 0.010543 0.299513
0.072753 0.010543 0.300487
0.073717 0.010683 0.300487
0.073717 0.010683 0.299513
0.073510 0.000646 0.290000
0.074001 0.000163 0.290000
0.074485 0.000654 0.290000
0.073993 0.001137 0.290000
0.073411 0.003898 0.296726
0.073444 0.003210 0.297416
0.074418 0.003257 0.297416
0.074384 0.003945 0.296726
0.072753 0.010543 0.300000
0.073235 0.010613 0.300487
0.073717 0.010683 0.300000
    
```

In addition, several other files get created in the process that are not listed here.

### 3.2 SELECTION OF THE CONDUCTOR

The conductor used in winding two layers of coil was similar to that was used in building a helical magnet for AGS at BNL. The key conductor parameters are given in Table 4.

**Table 4:** Key parameters of the superconductor used in the proof-of-principle dipole in Phase I.

|                           |            |
|---------------------------|------------|
| Filament diameter         | 10 microns |
| Wire diameter             | 0.33 mm    |
| Cu to Non-Cu ratio        | 2.5:1      |
| Cable type                | 6-around-1 |
| Cable diameter, bare      | 1 mm       |
| Cable diameter, insulated | 1.1 mm     |
| Cable $I_c$ @ 5T, 4.2 K   | 490 A      |

Phase II will use a similar conductor since the outer 8 layers of Phase II will be connected in series with the inner two layers of Phase I.

### 3.3 DESIGN OPTIMIZATION OF THE PROOF-OF-PRINCIPLE DIPOLE

The design of the proof-of-principle dipole used in the Phase I proposal was significantly upgraded. As mentioned earlier, while carrying out a more detailed design of 600 mm long B0ApF for Phase II and comparing it with the one mentioned in the Phase I proposal that was 150 mm long, major technical differences were observed due to length. Therefore, the length of two layers of the Phase I proof-of-principle coils were increased from 150 mm to 600 mm. Making the Phase I coils similar in length to the proposed Phase II inner coils, not only makes the Phase I coil more representative of the final magnet, but also allows them to be used for the inner two layers of the Phase II magnet.

The emphasis of the proof-of-principle dipole was to optimize the maximum achievable field integral (rather than the field quality) with representative spacers in the body of the magnet and representative spacers in the end of the magnet in each of the two layers of windings. The integrated field harmonics were kept within 10 units (computed at a 40 mm reference radius for a coil inner radius of 57 mm radius) so that they can be made small by optimizing the remaining 8 layers in Phase II.

The magnet also had an iron yoke over the coil. The inner radius of the yoke was 63.5 mm (5") and the outer radius was 114.3 mm (9").

The coil winding was optimized with the code ported and developed as the part of Phase I. We varied the number of turns in each layer along with the number of coil blocks in the body and in end of the magnet. The final choice was to have three blocks in the body and three in the ends in the each of two layers. Apart from the maximum integral field and field harmonics, an attempt was made to minimize the peak field in the body and in the end of the magnet.

The output of the program for the optimized design is given below:

| LAYER NO. | BLOCK NO. | TURN NO. | WEDGE (DEGREE)  | C2C-BODY (DEG) |
|-----------|-----------|----------|-----------------|----------------|
| 1         | 1         | 37       | 0.00000         | 0.00000        |
| 1         | 2         | 12       | 3.50000         | 0.18023        |
| 1         | 3         | 4        | 4.00000         | 0.51002        |
| LAYER NO. | BLOCK NO. | TURN NO. | END-SPACER (MM) | C2C-END (MM)   |
| 1         | 1         | 32       | 0.00000         | 0.00000        |
| 1         | 2         | 17       | 1.87098         | 0.18525        |
| 1         | 3         | 4        | 8.15469         | 0.49510        |
| LAYER NO. | BLOCK NO. | TURN NO. | WEDGE (DEGREE)  | C2C-BODY (DEG) |
| 2         | 1         | 28       | 0.00000         | 0.00000        |
| 2         | 2         | 13       | 2.53812         | 0.14090        |
| 2         | 3         | 5        | 4.97227         | 0.99809        |
| LAYER NO. | BLOCK NO. | TURN NO. | END-SPACER (MM) | C2C-END (MM)   |
| 2         | 1         | 23       | 0.00000         | 0.00000        |
| 2         | 2         | 15       | 1.47710         | 0.05291        |
| 2         | 3         | 8        | 20.79312        | 0.22348        |

CHI SQUARE = 250.17444252967834

INTEGRATED FIELD HARMONICS :

| No. | Bn(T.m)      | bn*10^4(units) | bn(des) | weight |
|-----|--------------|----------------|---------|--------|
| 0   | 0.57624E+00  | 10000.0000     | 0.0000  | 0.0000 |
| 2   | 0.73808E-04  | 1.2809         | 0.0000  | 1.0000 |
| 4   | -0.85596E-04 | -1.4854        | 0.0000  | 1.0000 |
| 6   | -0.39875E-03 | -6.9198        | 0.0000  | 2.0000 |
| 8   | -0.43460E-03 | -7.5421        | 0.0000  | 3.0000 |
| 10  | 0.25513E-03  | 4.4276         | 0.0000  | 4.0000 |
| 12  | -0.11341E-03 | -1.9682        | 0.0000  | 0.0000 |
| 14  | 0.14448E-04  | 0.2507         | 0.0000  | 0.0000 |
| 16  | 0.29303E-04  | 0.5085         | 0.0000  | 0.0000 |
| 18  | -0.56133E-05 | -0.0974        | 0.0000  | 0.0000 |
| 20  | -0.11768E-04 | -0.2042        | 0.0000  | 0.0000 |
| 22  | 0.47545E-05  | 0.0825         | 0.0000  | 0.0000 |
| 24  | -0.16136E-06 | -0.0028        | 0.0000  | 0.0000 |
| 26  | 0.12541E-05  | 0.0218         | 0.0000  | 0.0000 |
| 28  | -0.85662E-06 | -0.0149        | 0.0000  | 0.0000 |
| 30  | -0.14231E-06 | -0.0025        | 0.0000  | 0.0000 |

The program also creates a conductor file that can be imported into OPERA3d for further analysis. Fig. 11 shows the coil (red) created from that inside an iron yoke (green).

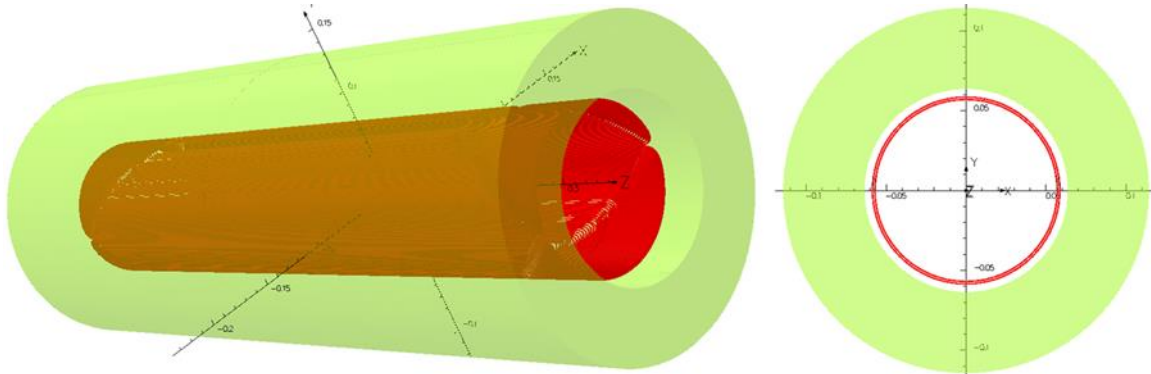


Figure 11: Two views of the OPERA3D model of the optimum integral dipole as built. The coil is shown in red and the iron in green. The model on the right shows the view from the end.

Fig. 12 shows the field over the coil and iron after the OPERA3d model was solved and analyzed at a current of 920 A.

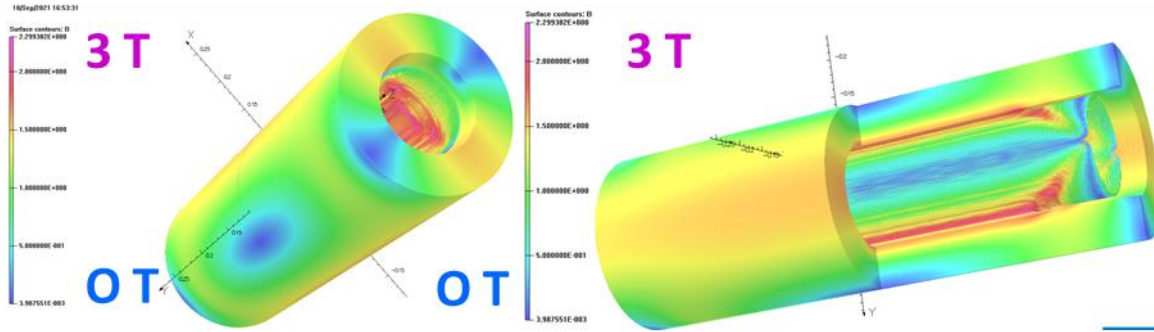


Figure 12: Two views of the OPERA3D model of the optimum integral dipole as built with field superimposed over the coil and the iron at 920 A. The view on the right shows  $\frac{3}{4}$  of the iron for clarity.

To visualize the field over the coil more clearly, the left side of Fig. 13 shows only half of the coil with field superimposed over it. (There is yoke included in arriving at the solution on the other half of the coil, but it is hidden from the display.) The right side of Fig. 13 shows the field on the axis, including the field outside the magnet.

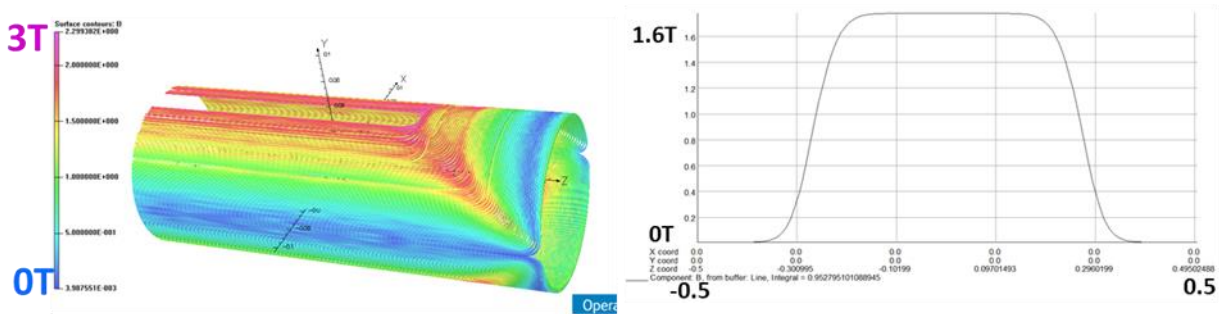


Figure 13: The picture on the left shows the field superimposed over the coil. Half of the coil and the iron are hidden for clarity. The picture on the right shows the computed field at 920 A. One can clearly see that the midplane turns are extended almost to the entire coil length, the key advantage of the optimum integral design over the other end designs in creating a higher field in the optimum integral design.

The key parameters of the optimum integral dipole as designed for the Phase I are given in Table 5.

**Table 5:** Key Parameters of the Phase I proof-of-principle optimum integral dipole

|                  |              |
|------------------|--------------|
| Coil Aperture    | 114 mm       |
| Quench Field     | 1.7 T        |
| Peak Field       | 2.2 T        |
| Coil Length      | 0.6 m        |
| Number of Layers | 2            |
| Number of turns  | 99           |
| Stored Energy    | 7.5 k Joules |

### 3.4 WINDING OF THE PROOF-OF-PRINCIPLE OPTIMUM INTEGRAL DIPOLE COIL

Winding of the proof-of-principle optimum integral dipole coil was the most expensive, time consuming, and critical task of the Phase I. One of several goals was to minimize the bend radius at the end while maintaining a good quality

of coil winding. Several practice coils, as shown in Fig. 14, were wound to determine optimum parameters. Only a few critical turns were wound for iterating the key parameters. One can also see in the background of Fig. 15 an insulated tube for winding the full-length coil at the second winding station.

The pictures in Fig. 15 show the process of winding the full-length practice coil. The picture on Fig. 15(left) shows the stainless-steel tube installed for winding the coil. The picture on Fig. 15 (right) shows a snapshot of the practice coil. The winding for each layer starts from the pole turn at one-half of the coil, proceeds to the midplane, and then to the pole of the other half of the coil. This avoids a splice between the two coil halves.

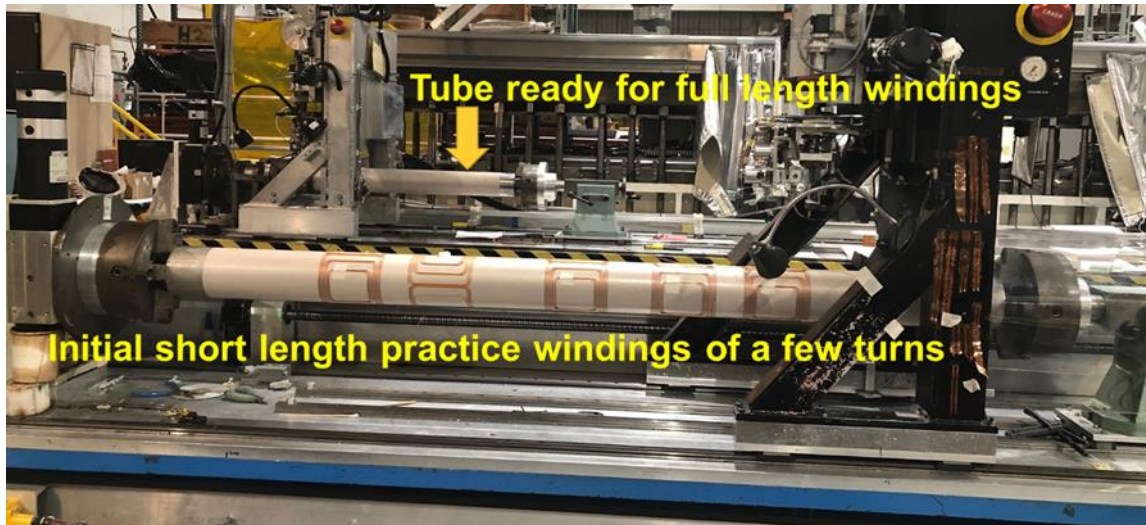


Figure 14: Initial practice winding of several short coils (a few turns only) for iterating the winding parameters. Shown in the background is an insulated tube ready of winding the full-length coil.

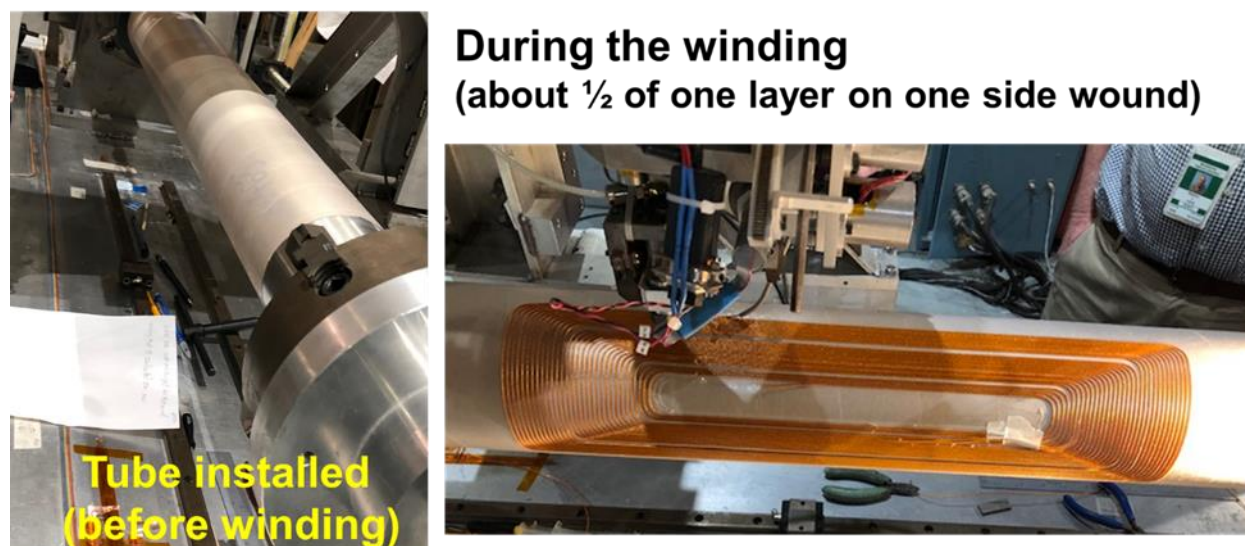


Figure 15: The picture on the left shows the tube installed for winding the coils; the picture on the right shows winding of the full-length practice coil. Winding for each layer starts from the pole turn of one-half of the coil, proceeding to the midplane, and then to the pole of the other half; thus avoiding a splice.

Fig. 16 shows series of pictures of more details of the winding of the coil and ongoing discussion between the PBL and BNL team members during the full-length practice winding. The picture on the bottom right zooms in on how the superconducting wire is laid and bonded with the ultrasound on the substrate.

## BNL and PBL staff during the initial part of full-length practice winding



Figure 16: A series of pictures shows more details of the winding of the full-length practice coil. The picture on the bottom right zooms in to show how the superconducting wire is laid and bonded with the ultrasound on the substrate.

The winding of the proof-of-principle optimum integral dipole to create the highest possible field in Phase I for the given length started after the process and parameters were optimized. The remaining section describes the series of steps involved in completing the construction of this magnet. Fig. 17 shows the Kapton wrap on the stainless-steel tube and Fig. 18 shows the Fiberglass wrap on the Kapton in preparation for winding of the Phase I coil.

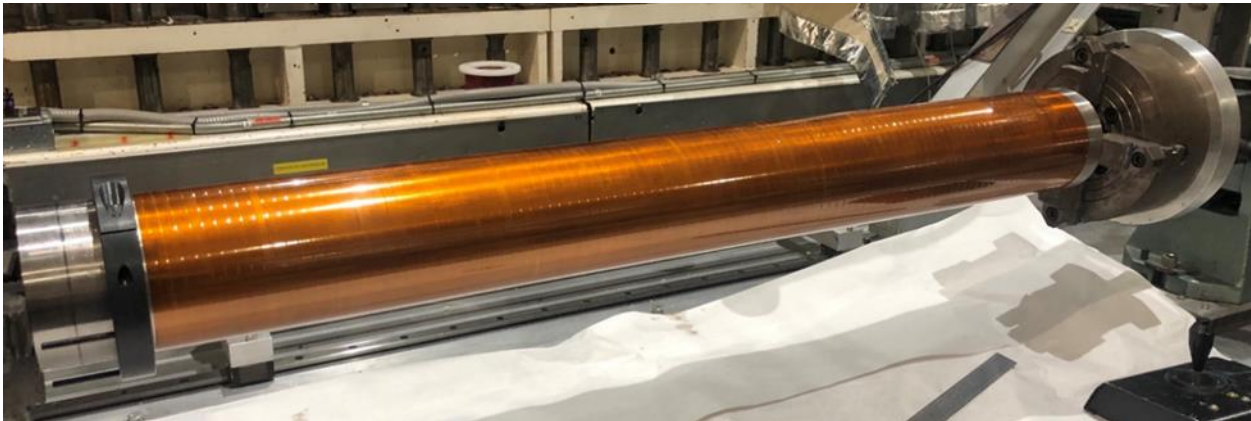


Figure 17: Kapton wrap on the stainless-steel tube in preparation for winding of the Phase I coil.



Figure 18: Fiberglass wrap on the Kapton in preparation for winding of the Phase I coil.

Fig. 19 shows two views of the winding of the first layer of the proof-of-principle coil for the Phase I. Fig. 20 zooms in over two ends to show them more clearly.

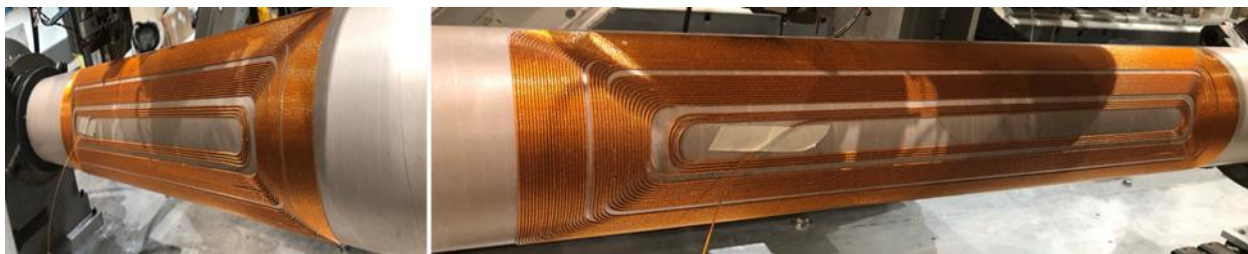


Figure 19: Views of the first layer of the proof-of-principle coil during the winding.

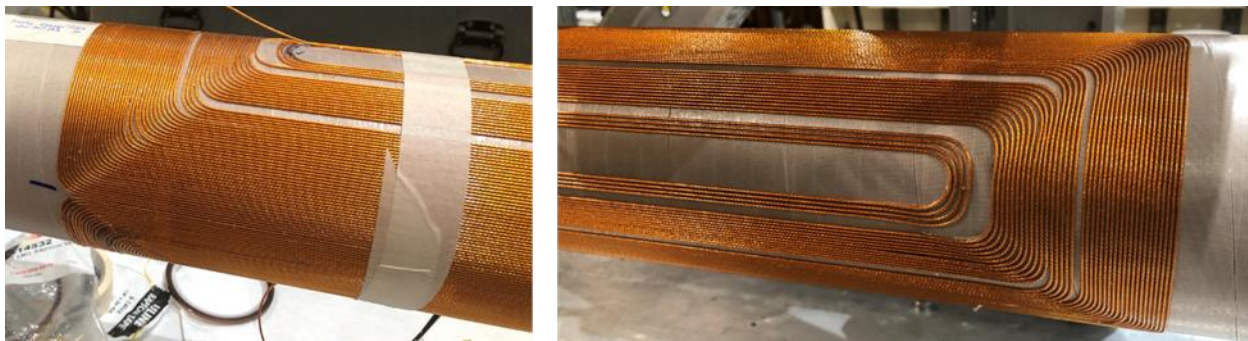


Figure 20: Pictures of the two ends of the first layer of the proof-of-principle coil during the winding.

Fig. 21 shows the voltage tap install at the pole exit from the first layer of the proof-of-principle coil.

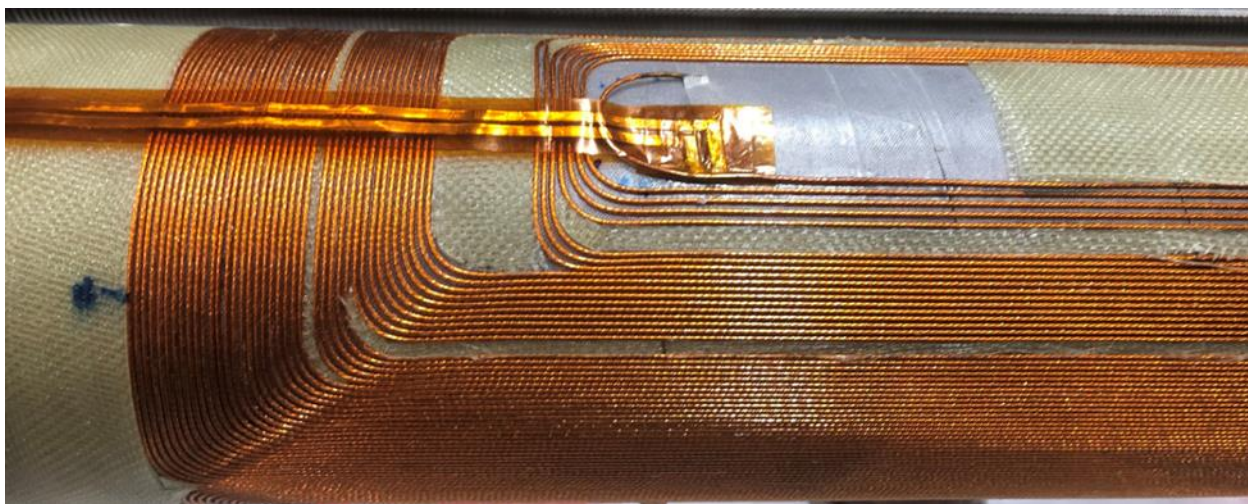


Figure 21: Voltage tap install at the pole exit from the first layer of the proof-of-principle coil.

Fig. 22 shows a coat of the blue epoxy after filling the gaps in the coil winding that were left for the body and end spacers.

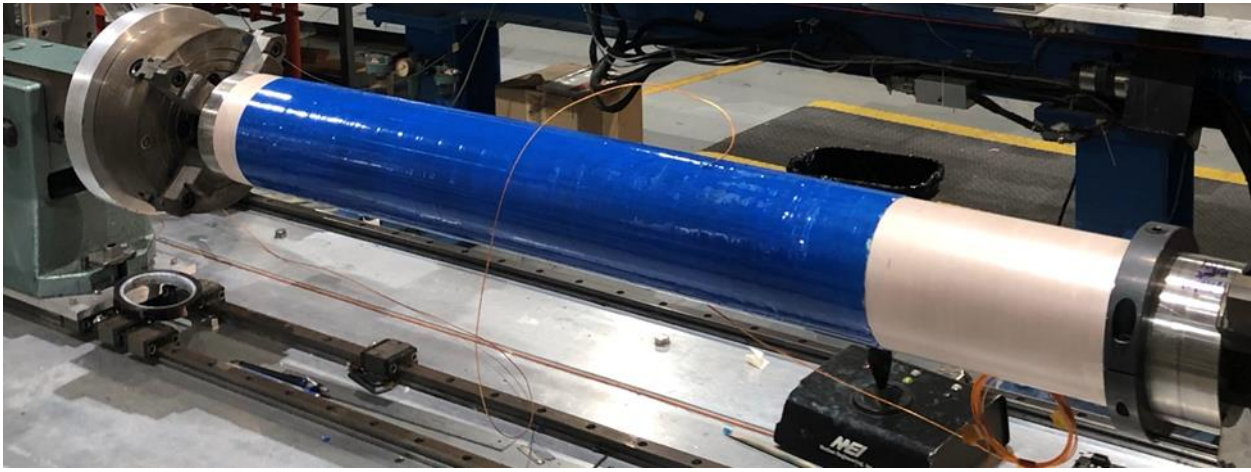


Figure 22: A coat of the blue epoxy after filling the gaps in the coil winding that were left for the body and end spacers.

Fig. 23 shows a snapshot during the winding of the second layer of the coil. One can appreciate from this picture how far the midplane turns are extended which is the key to creating more field in the optimum integral design over the conventional end design.

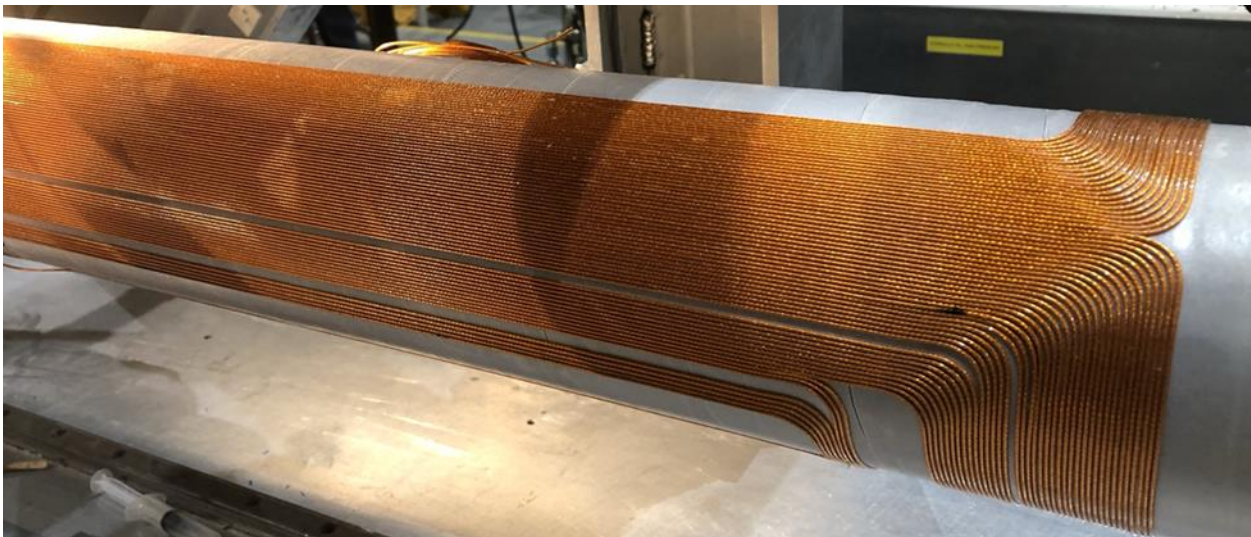


Figure 23: Second layer of the optimum integral design being wound.

The picture in Fig. 24 is taken after the winding of the second layer was complete. The photo shows start and exit lead V-Taps. Fig. 25 shows the picture of the completed coil getting ready for the cure.



Figure 24: Second layer wound. Voltage-tap wires installed at the start and exit leads.



Figure 25: Two layers of coils getting ready for the final cure.

Fig. 26 shows the optimum integral coil for the proof-of-principle dipole with multiple layers of Fiberglass roving providing necessary pre-tension after the final cure.



Figure 26: Optimum integral proof-of-principle dipole coil with Fiberglass roving providing necessary pre-tension after the final cure.

Fig. 27 shows the optimum integral coil placed inside the iron yoke ready for test. The magnet has a simple cylindrical yoke with an inner diameter of 5 inches (127 mm) and outer diameter of 9 inches (228.6 mm) and a length of 26" (660.4 mm). The construction of the magnet with two layers of coil wound and placed inside the iron yoke was a key Phase I deliverable.

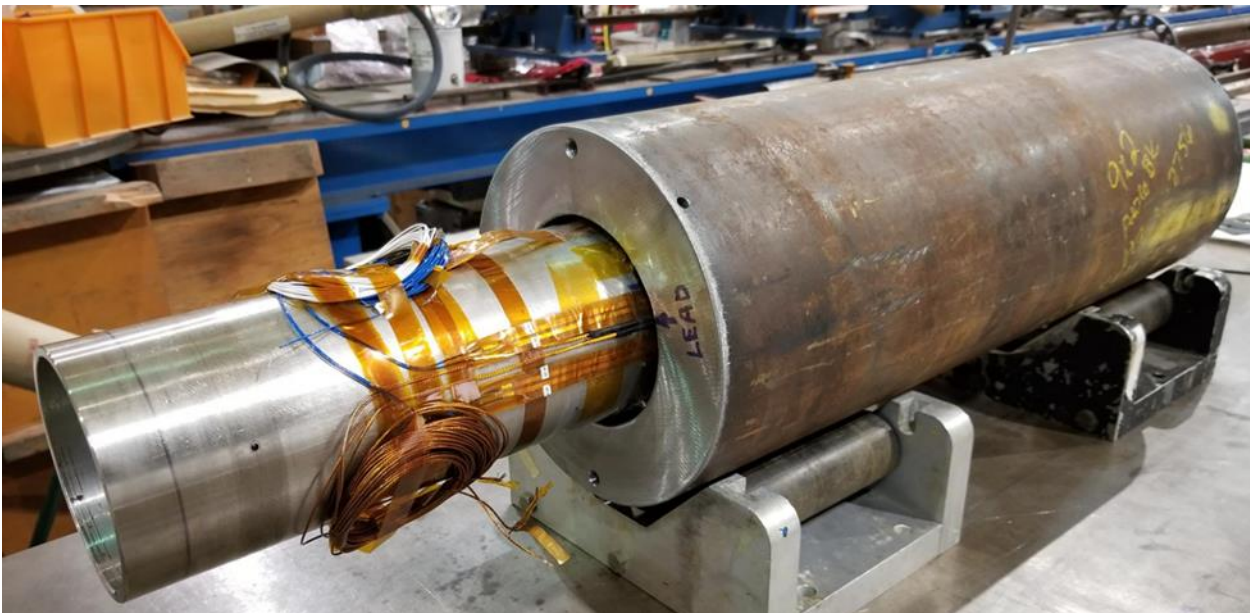


Figure 27: Optimum integral proof-of-principle coil inside the iron yoke completed as a part of key Phase I deliverable.

### 3.5 PREPARATION OF THE PROOF-OF-PRINCIPLE DIPOLE FOR A 4 K TEST

The magnet was high-potted and various QA tests on the coil were performed as a part of preparation for the 4 K test. Fig. 28 shows the magnet getting prepared with all electrical and instrumentation connections and with the top-hat for the 4K test.

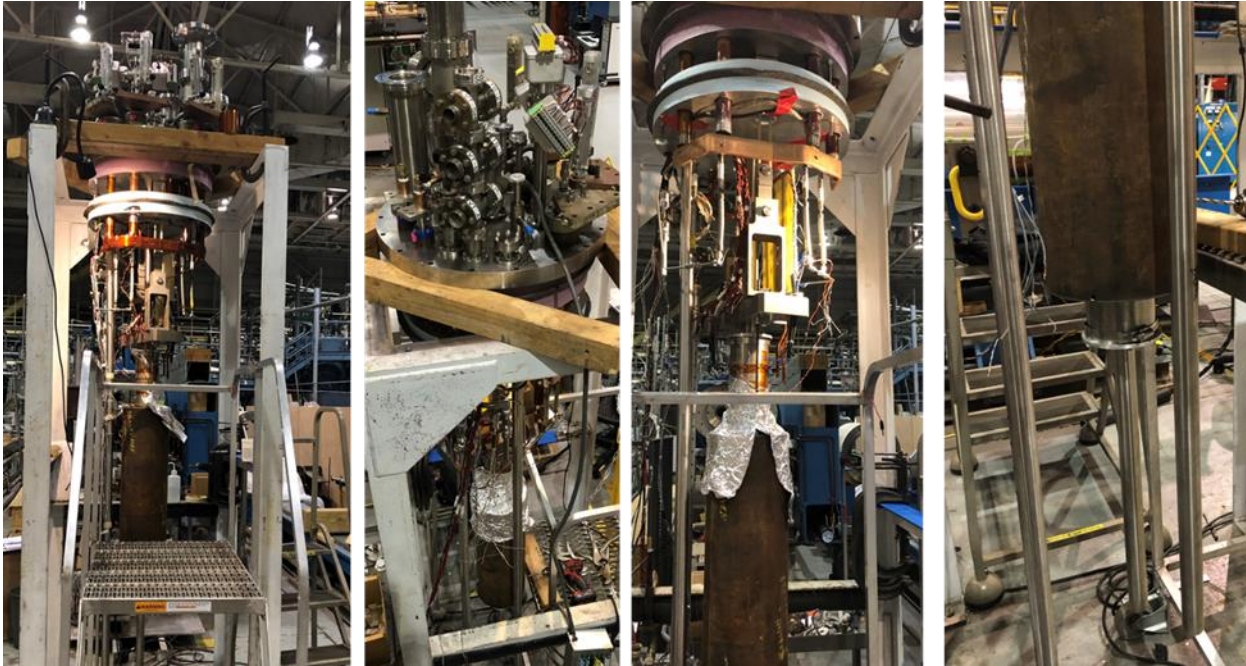


Figure 28: Optimum integral dipole getting ready with all electrical and instrumentation connections and with the top-hat for the 4K test.

### 3.6 PROOF-OF-PRINCIPLE DIPOLE TEST AT 4 K

One of the most important achievements of the Phase I work was the demonstration of the proof-of-principle optimum integral dipole with a 4 K test. The magnet was placed in the Dewar 6 (see Fig. 29 left). Fig 29 (right) shows the team at the BNL superconducting magnet division performing the test. It was a short test and magnet reached the short sample (see Fig. 30).

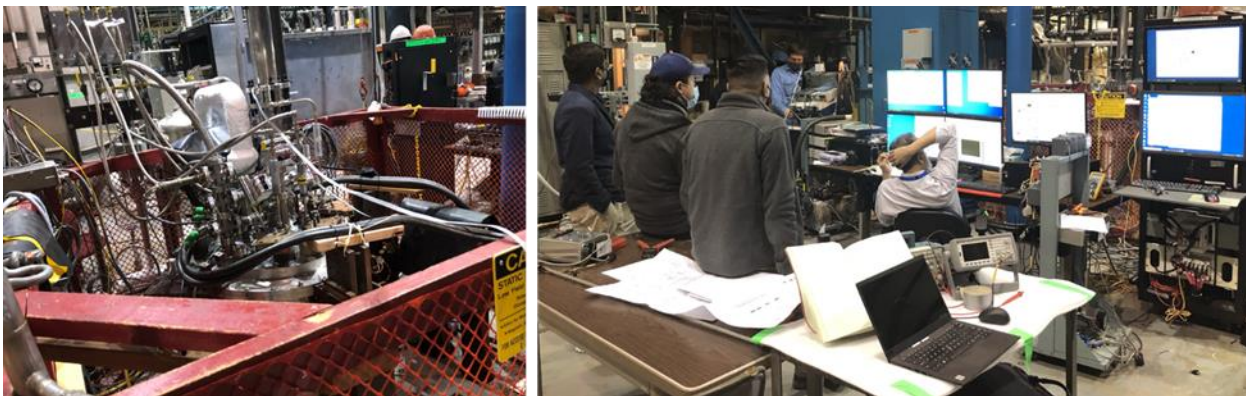


Figure 29: Picture on the left shows the optimum integral dipole in Dewar 6 and the picture on the right shows the BNL team performing the 4 K test in liquid Helium.

The magnet reached the plateau at current of reached at a current of  $\sim 868$  A after the first quench at 860 A. A couple of test run were also carried out to study the ramp rate effects on the quench performance that was anticipated for the 6-around-1 cable. The magnet will not be ramped in EIC at such high ramp rates and was merely an academic exercise for this purpose.

This is a significant demonstration of the technology in Phase I showing that a 114 mm aperture magnet reaching a field of  $\sim 1.7$  T field (peak field on conductor  $\sim 2.2$  T), essentially after one quench which itself was very close to plateau. The exact cable performance is not known since it was a leftover (spare) conductor. The computed quench field was essentially the same that predicted for a similar conductor.

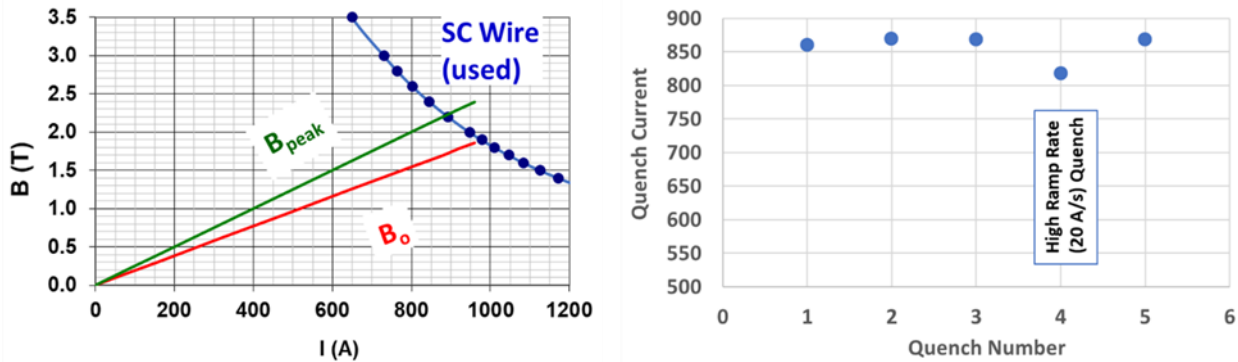


Figure 30: Left: Computation of the quench current, peak field on the conductor and the field at the center of the magnet for a conductor similar to the one used in the Phase I dipole. Right: Quench current for the first five quenches. Magnet reached the quench current of  $\sim 868$  A after the first quench at 860 A. Ramp rate dependence can be seen at a high ramp rate (higher than that required in EIC) as the magnet quenched at 818 A when the ramp rate was 20 A/s.

### 3.7 COMPARISON BETWEEN CALCULATIONS AND MEASUREMENTS IN THE PROOF-OF-PRINCIPLE DIPOLE

We compare the measurement of the field along the axis with the calculations. This is an important evaluation of the claim that the optimum integral coil design can extend the high field region in the magnet. It was not a part of the test scheduled in Phase I but was carried out at room temperature (a low-cost test) given the importance of it. Fig. 31 compares the measurements and calculations at a current of 2 A. The calculations are shown with a solid blue line and the measurements are shown with an open red circle. A good agreement between the two shows the promise of the optimum integral design.

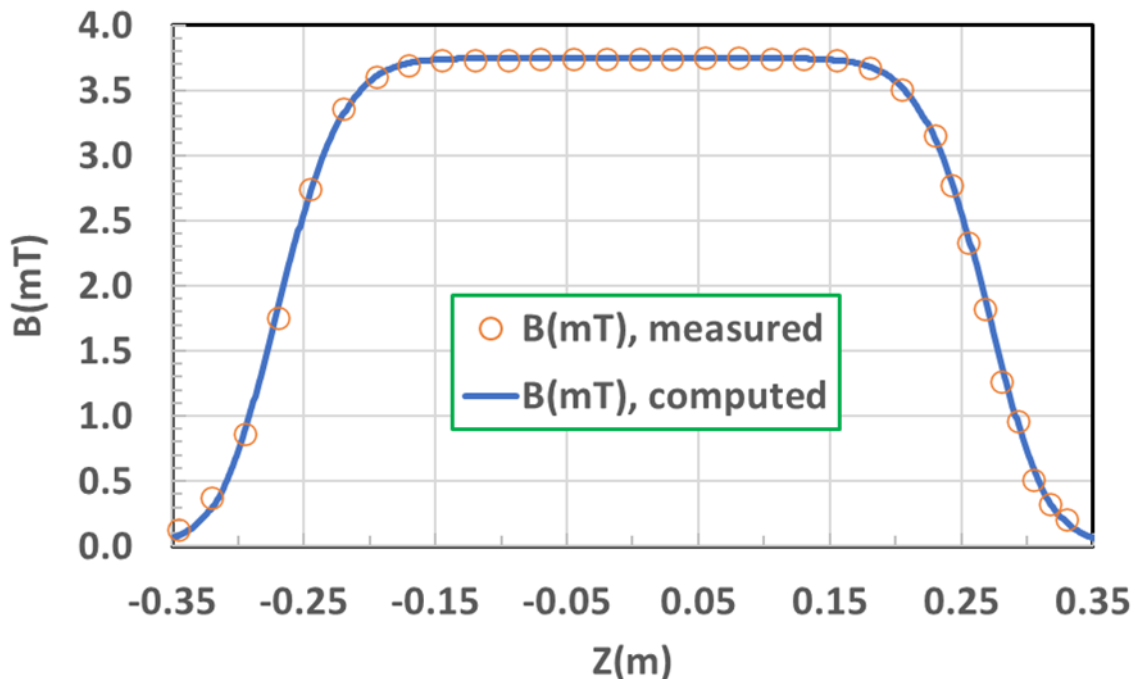


Figure 31: A comparison between the calculations (solid blue line) and measurements (open red circle) at a current of 2 A. A good agreement between the two shows the promise of the optimum integral design.

### 3.8 MAGNETIC, MECHANICAL AND WINDING OPTIMIZATION FOR THE PHASE II MAGNET

The initial overall design of the magnet that is being proposed to be built in Phase II has been developed. This includes the winding optimization, magnetic analysis, and mechanical analysis. Further analysis and optimization will continue during the early part of Phase II.

#### 3.8.1 Magnetic Design and Analysis

The Phase II magnet will consist of 10 layers of direct wind, 600 mm long coils based on the optimum integral design. It will use 2 layers already built and tested in Phase I. The Phase II magnet is designed to provide a good field quality with all harmonics meeting the current specifications. It is also designed to deal with the Lorentz forces that are expected in this magnet when energized to the design field. The pre-stress on the coil will be provided with the pre-tension in the Fibergalss, which is efficient against the radial Lorentz forces. In addition, three stainless steel tubes - two inner tubes on which the coils are wound (including the one which was part of Phase I), and one over the entire 10-layer coil set, will control the bending and provide additional support to keep deflections in the coil within acceptable limits.

The initial parameters of the Phase II B0ApF dipole based on the optimum integral design are given in Table 6.

**Table 6:** Key Parameters of the Phase I proof-of-principle optimum integral dipole

|                  |             |
|------------------|-------------|
| Coil Aperture    | 114 mm      |
| Design Field     | 3.8 T       |
| Peak Field       | 4.2 T       |
| Coil Length      | 0.6 m       |
| Number of Layers | 10          |
| Number of turns  | 499         |
| Stored Energy    | 58 k Joules |

The field harmonics are optimized with the program being developed as a part of this program. The optimization of the optimum integral coil had to be carried out in two parts to work within the limits of the current program (the program will be further upgraded in Phase II to do all optimizations together). See below the optimized harmonics in two parts. The first part is for six inner layers (left) and the second for the outer four (right).

### Six inner layers

INTEGRATED FIELD HARMONICS :

| No. | Bn(T.m)      | bn*10 <sup>4</sup> (units) |
|-----|--------------|----------------------------|
| 0   | 0.10784E+01  | 10000.0000                 |
| 2   | -0.16778E-03 | -1.5559                    |
| 4   | -0.20092E-03 | -1.8631                    |
| 6   | -0.31637E-04 | -0.2934                    |
| 8   | 0.11920E-03  | 1.1053                     |
| 10  | 0.16403E-03  | 1.5210                     |
| 12  | -0.10239E-03 | -0.9494                    |
| 14  | 0.23144E-04  | 0.2146                     |
| 16  | 0.41950E-05  | 0.0389                     |
| 18  | -0.83516E-06 | -0.0077                    |
| 20  | -0.26621E-05 | -0.0247                    |
| 22  | 0.73377E-06  | 0.0068                     |
| 24  | 0.13543E-06  | 0.0013                     |
| 26  | 0.17462E-06  | 0.0016                     |
| 28  | -0.13758E-06 | -0.0013                    |
| 30  | -0.14597E-07 | -0.0001                    |

### Four outer layers

INTEGRATED FIELD HARMONICS :

| No. | Bn(T.m)      | bn*10 <sup>4</sup> (units) |
|-----|--------------|----------------------------|
| 0   | 0.84286E+00  | 10000.0000                 |
| 2   | 0.10652E-04  | 0.1264                     |
| 4   | 0.71433E-06  | 0.0085                     |
| 6   | 0.55433E-05  | 0.0658                     |
| 8   | -0.14826E-04 | -0.1759                    |
| 10  | 0.10565E-04  | 0.1254                     |
| 12  | -0.36202E-05 | -0.0430                    |
| 14  | 0.75101E-06  | 0.0089                     |
| 16  | -0.47847E-07 | -0.0006                    |
| 18  | -0.61086E-08 | -0.0001                    |
| 20  | -0.27374E-08 | -0.0000                    |
| 22  | 0.10323E-09  | 0.0000                     |
| 24  | 0.19501E-09  | 0.0000                     |
| 26  | 0.23912E-10  | 0.0000                     |
| 28  | -0.60265E-11 | -0.0000                    |
| 30  | -0.77363E-11 | -0.0000                    |

The optimization above is only representative and the actual optimization of the magnet in Phase II will get feedback from measured field errors (warm) in the previous layers.

Fig. 32 shows the initial magnetic design of the Phase II B0ApF optimum integral dipole. The left side shows the complete 3-d view with coils in red and iron in green (transparent) and the right side shows a view from the end. Fig. 33 shows the field contour superimposed over the coil and iron and Fig. 34 shows the iron hidden for more clarity to visualize the field on the surface of the coil.

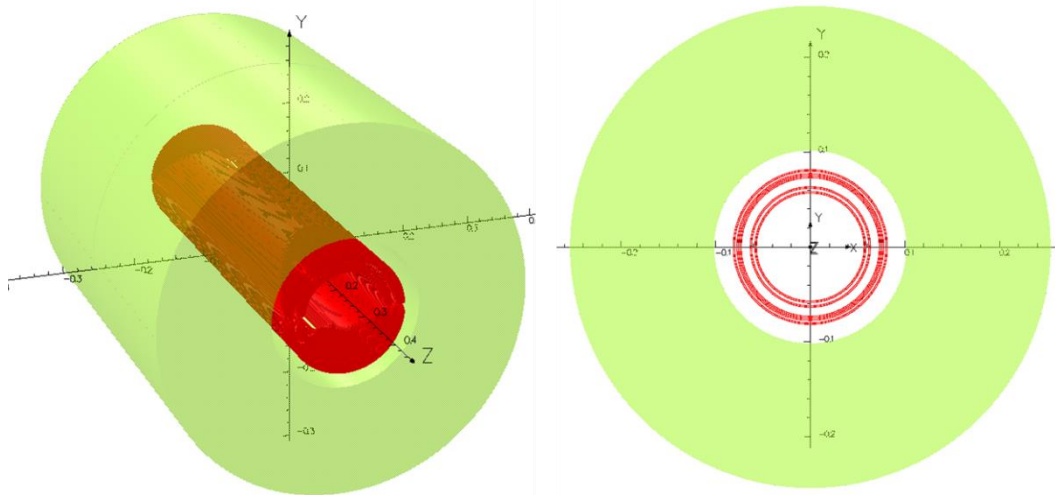


Figure 32: Initial magnetic design of the Phase II B0ApF optimum integral dipole. Left: a 3-d view of coils in red and iron in green (transparent); Right: a view from the end.

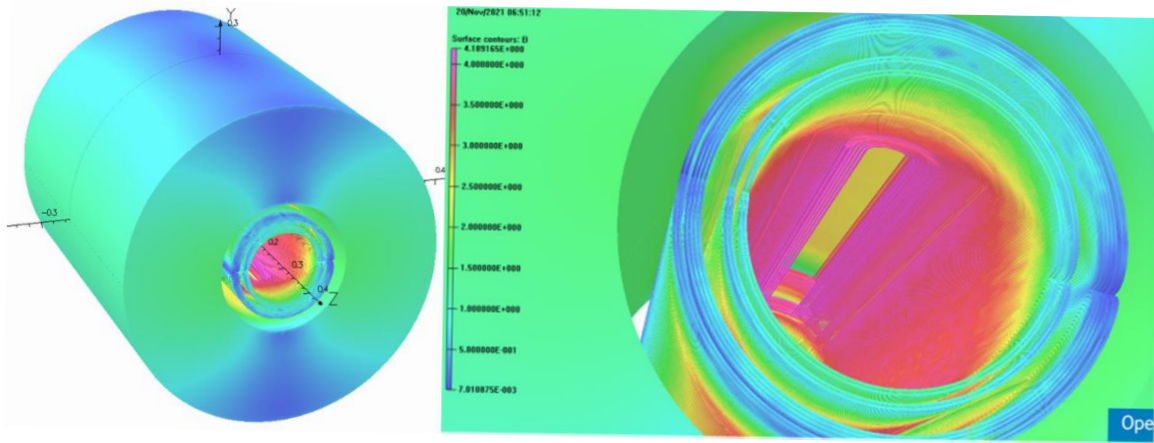


Figure 33: Field contours superimposed over the surface of the iron and coil. Left: entire magnet; Right: a zoomed in model to visualize the field in the coil.

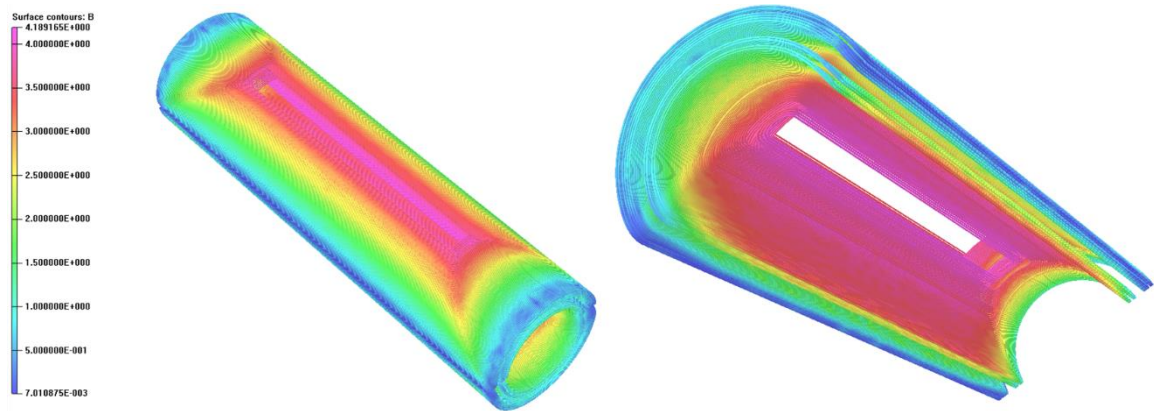


Figure 34: Field contours superimposed over the surface of the coil. Iron is hidden to better visualize the peak field on the coil.

### Mechanical Analysis

A mechanical analysis was performed for several cases with the code COMSOL and ANSYS and will continue in more detail in Phase II. We first present the results of analysis performed with COMSOL and then with ANSYS.

#### 3.8.2 Mechanical Analysis with COMSOL

Fig. 35 shows the mechanical analysis with COMSOL of the bonded structure of the coil divided in two with the inner and outer coils having 10 mm and 15 mm of stainless-steel tube over them.

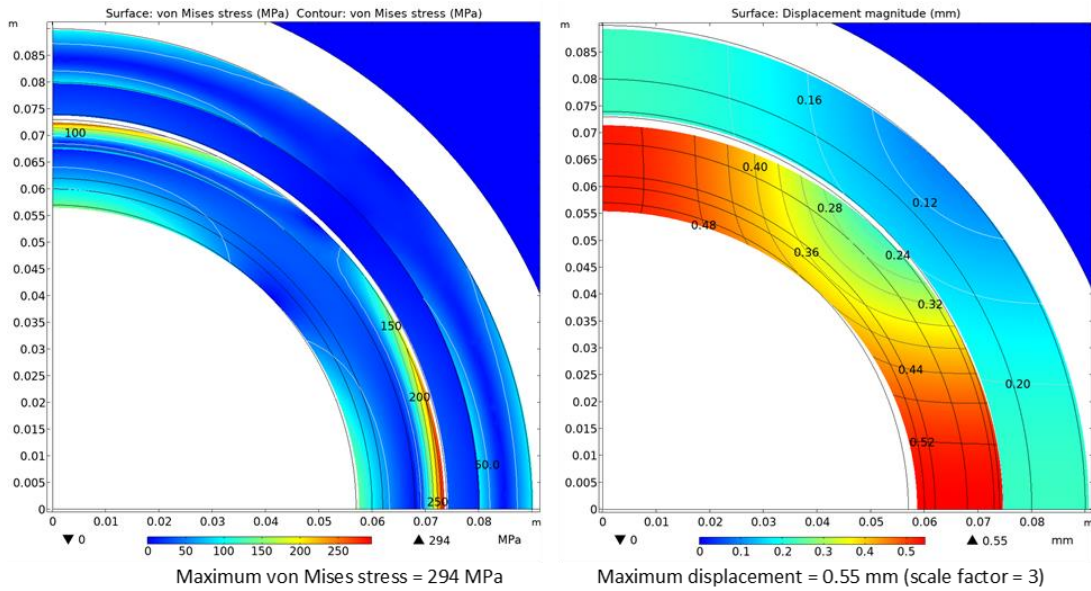


Figure 35: von Mises stresses on the coil and intermediate tube and deflections for the case of a boned structure with two stainless steel tubes (10 mm and 15 mm).

Fig. 36 shows the results of magnetic (left) and mechanical analysis (right) with the code COMSOL of a 4-layer inner coil and a 6-layer outer coil. Each coil has steel reinforcement both inside and outside, 10 mm thick, to function like the flanges of a beam to improve bending stiffness.

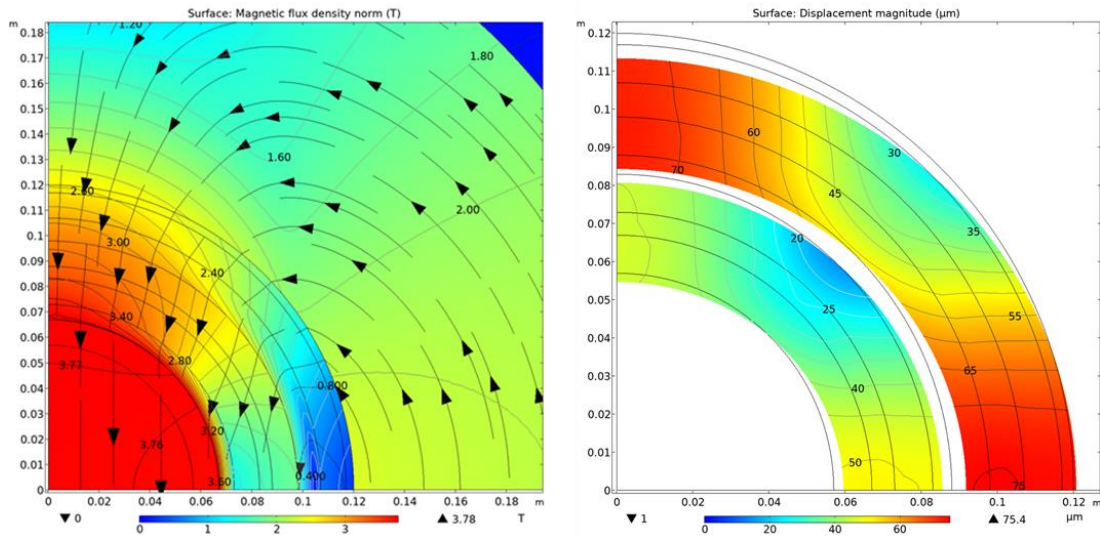


Figure 36: Magnetic (left) and mechanical analysis of a 4-layer inner and a 6-layer outer coil with 10 mm thick inner and outer stainless-steel tubes.  $E_{Sst} = 219$  GPa;  $E_{coil} = 33$  GPa, Inner  $\delta_{max} = 50$   $\mu$ ; Outer  $\delta_{max} = 75$   $\mu$ ; Displacements magnified 50 times.

Various mechanical design options (such as the one analyzed here) will be compared against the baseline option of three stainless steel tubes with pre-tension provided by the fiberglass roving.

### 3.8.3 Mechanical Analysis with ANSYS

#### Geometry of Proposed Optimized Dipole:

Figure 37 displays the geometry of the dipole magnet cross section model. The colors in figure 37 regions are defined in Table 1. The gaps in the coils are ignored and a single block is used for each layer. The ignored gaps are of the order of a few degrees and would not have a significant effect on the fields. A steel yoke is added to capture the far magnetic field. Table 1 shows the mechanical parameters used in the structural analysis.

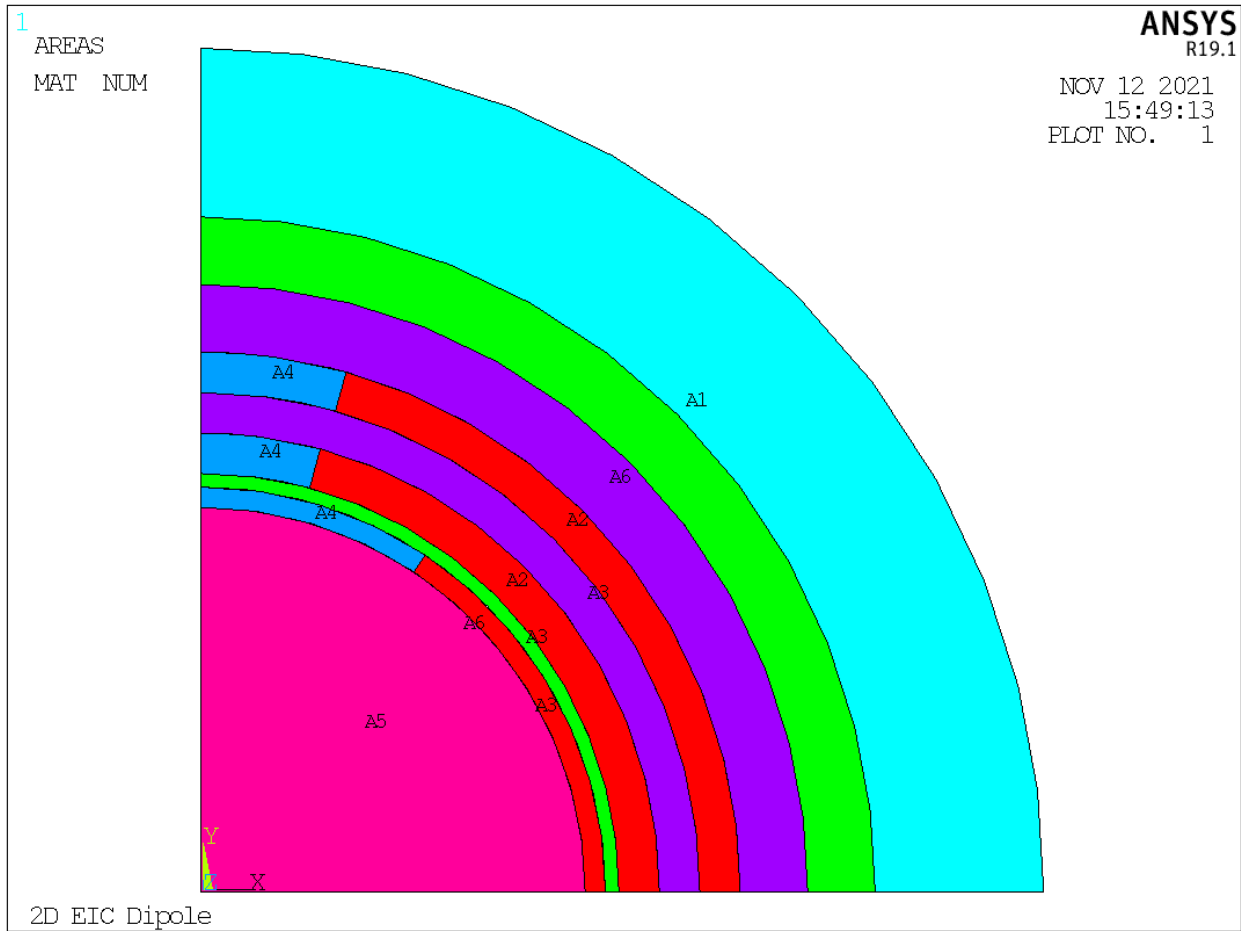


Figure 37: 2D cross section geometry of magnet. Colors show the different materials.

| MATERIAL    | COLOR      | COMMENT                     | YOUNG'S MODULUS | POISSON RATIO |
|-------------|------------|-----------------------------|-----------------|---------------|
| COIL        | Red        | G10 parameters              | 17.5 GPa        | 0.3           |
| POLE WEDGE  | Light Blue | G10 parameters              | 17.5 GPa        | 0.3           |
| SS 304      | Violet     |                             | 193 GPa         | 0.25          |
| INSULATION  | Green      | Interleaving between layers | 73 GPa          | 0.3           |
| LOW C STEEL | Cyan       | Contain Field               | 207 GPa         | 0.3           |
| AIR         | Rose       | Aperture                    | NA              | NA            |

Table 7: Description of colors on Figure 37.

**Field Calculation:**

A field calculation is performed in ANSYS to provide the nodal Lorentz forces to be used in the structural analysis. For these calculations it is assumed that the current density in the coils is 500 A/mm<sup>2</sup>. This is close to 500 A per wire. Figure 38 shows the field, B<sub>mod</sub>, calculated in ANSYS. The field in the aperture is ~3.5 T. A plot of the vector potential is shown in Figure 39. There is some curvature present in the aperture field which may indicate higher order harmonics are present. Figure 40 shows the field contour plot from OPERA2D as a validity check of the ANSYS field. Opera shows that the peak field is in the SS whereas ANSYS shows it in the Iron yoke. It should be noted that the BH curve is different for the two programs. Figure 41 shows the potential contour for Opera2D which looks similar to the ANSYS contours.

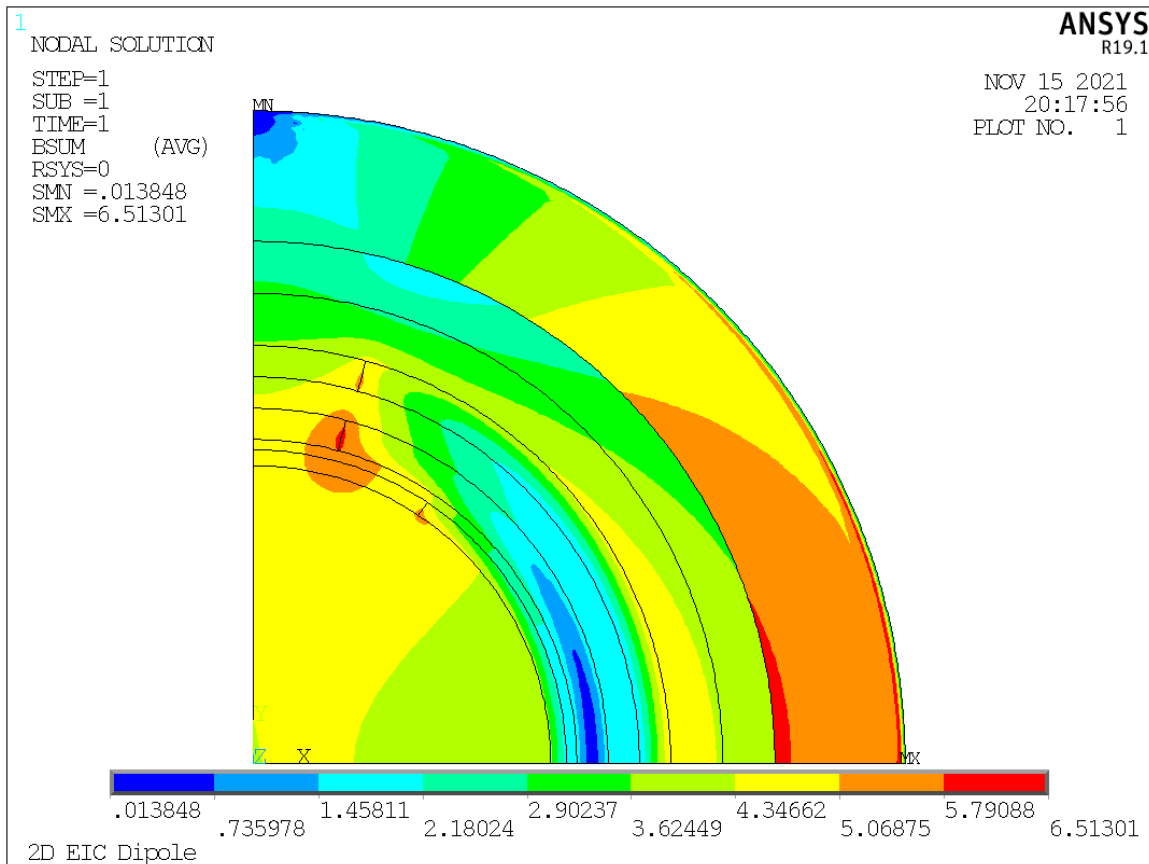


Figure 38: Field contour plot from ANSYS to be used for the forces for the structural analysis.

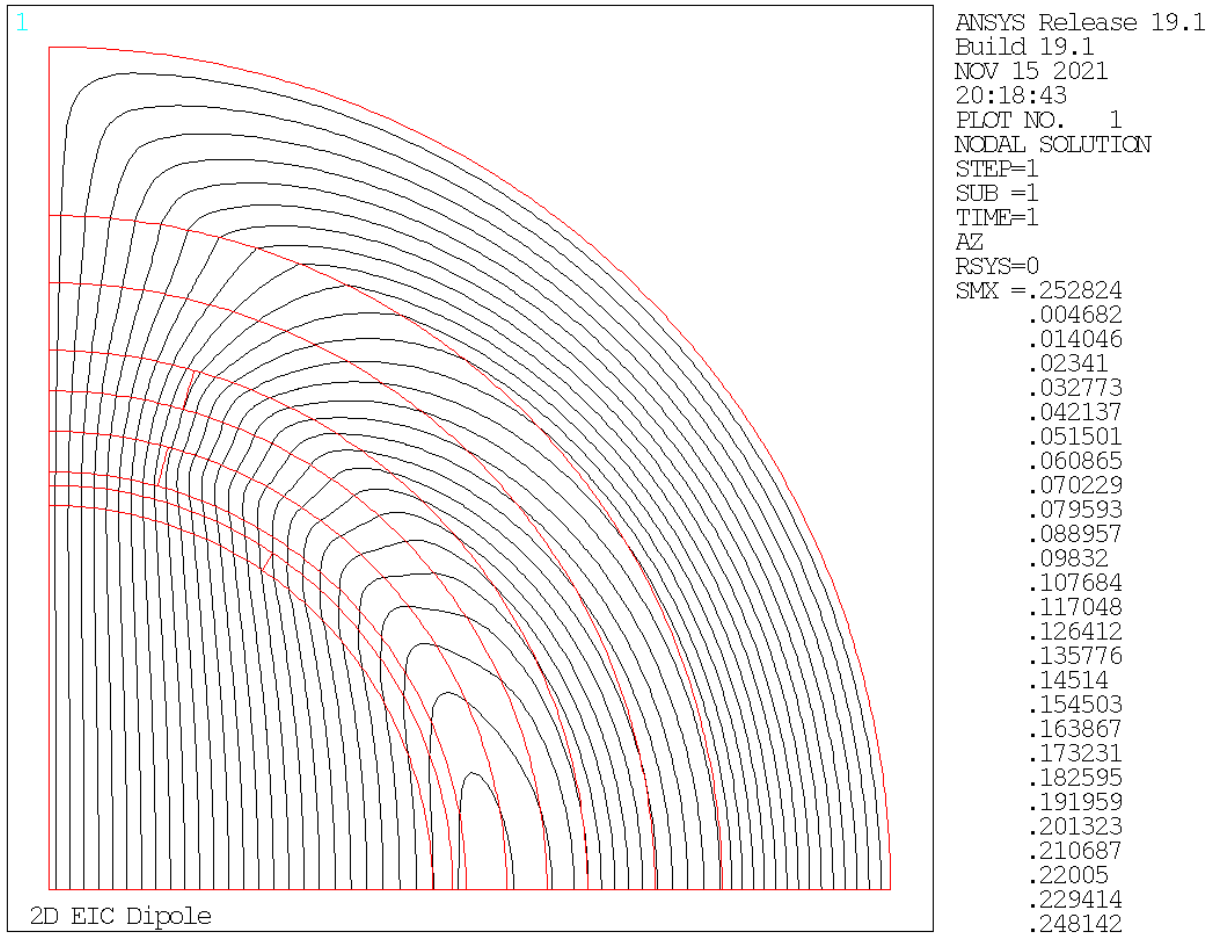


Figure 39: Contour plot of Az

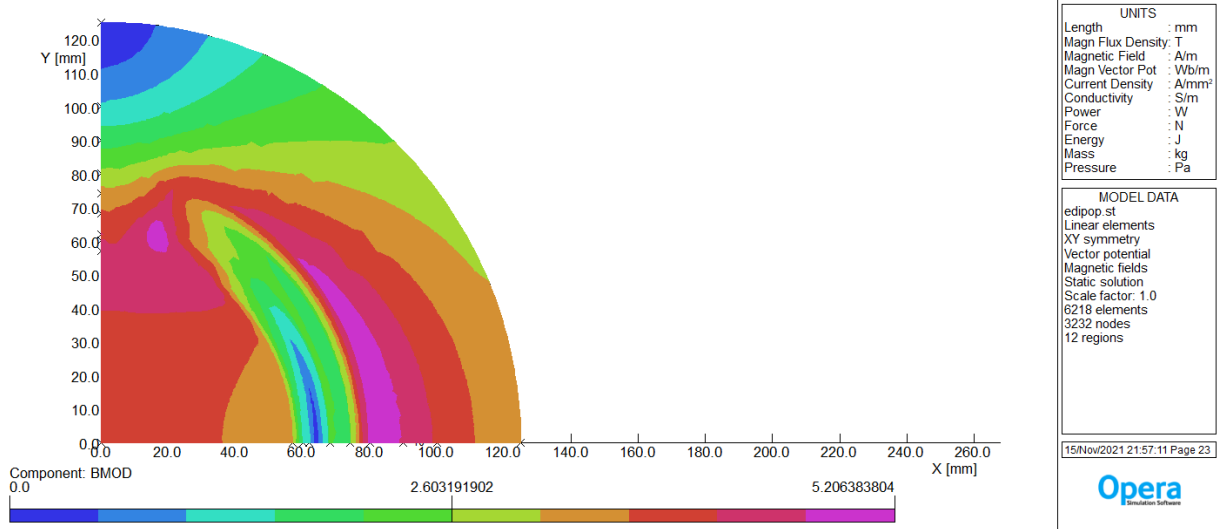


Figure 40: Field Contour plot from Opera 2D.

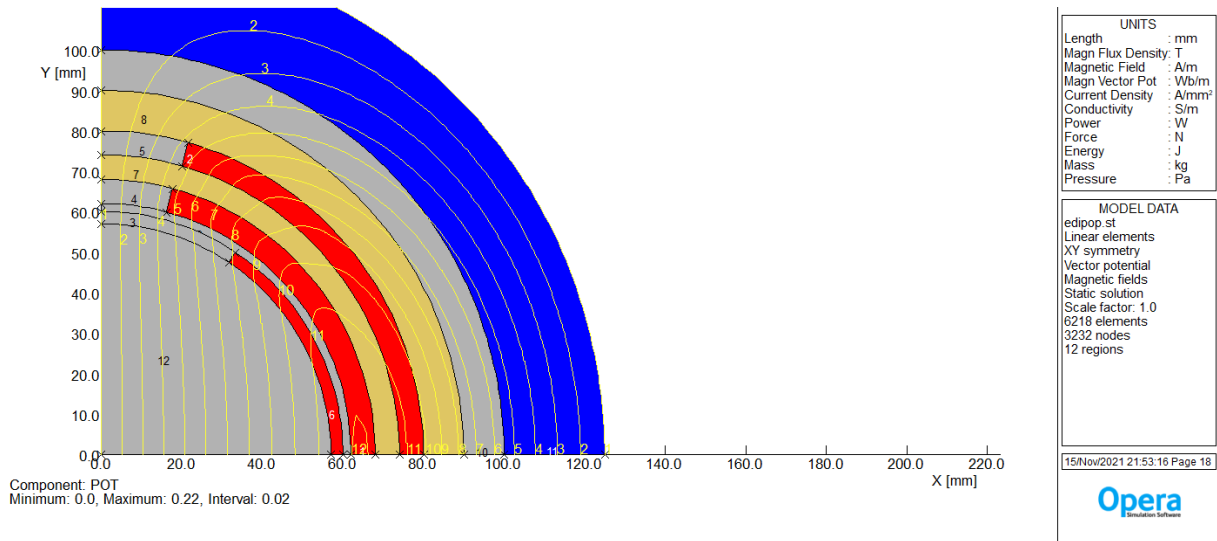


Figure 41: Contour plots of Az from the OPERA2D analysis.

### **Structural Calculations:**

#### **Case 1 Original Design: 2-4-4 Configuration**

The structural analysis used the Lorentz forces previously calculated. The force at each node in the coils is written by ANSYS in the EM FE analysis. The structural analysis uses the same nodal structure, with 8 node planar elements but with different element types. This initial case has a *super layer* configuration comprised of 2, 4, 4 layers where the layers in each *super layer* the same block structure. The 4 *super layers* are supported at the outside with a stainless-steel tube which is shown as yellow regions in Figure 41. Figure 42 shows the contour plot of displacements. The largest displacement occurs at the inner coil near the pole with maximum displacement is 201  $\mu\text{m}$ . This should not be a concern.

Figure 43 shows the Von Mises stress. The maximum stress is 328 MPa which occurs at the outer coil (layers 7 through 10) near the pole. Figure 44 shows the strain corresponding to the Von Mises stress. The maximum strain is 0.36% which also occurs in the outer coil near the pole. Figure 45 shows the Von Mises strain in the coils.

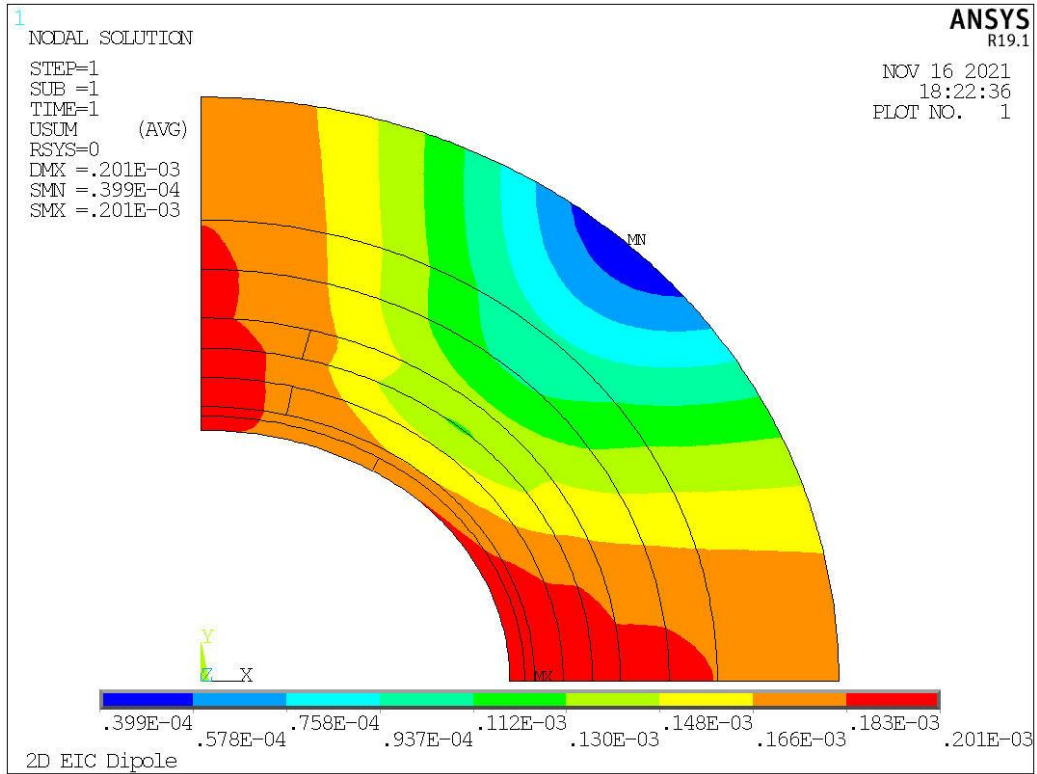


Figure 42: Displacement contour plot in meters. The maximum displacement in this case is 0.201 mm or 201 μm.

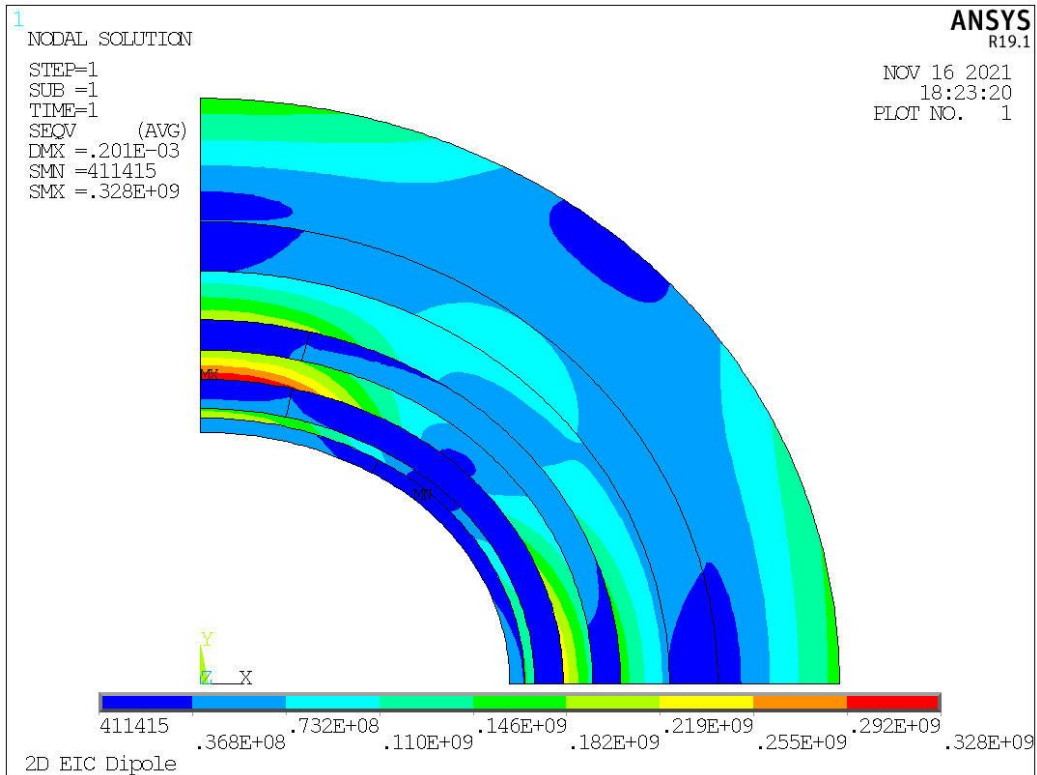


Figure 43: Von Mises stress contour plot

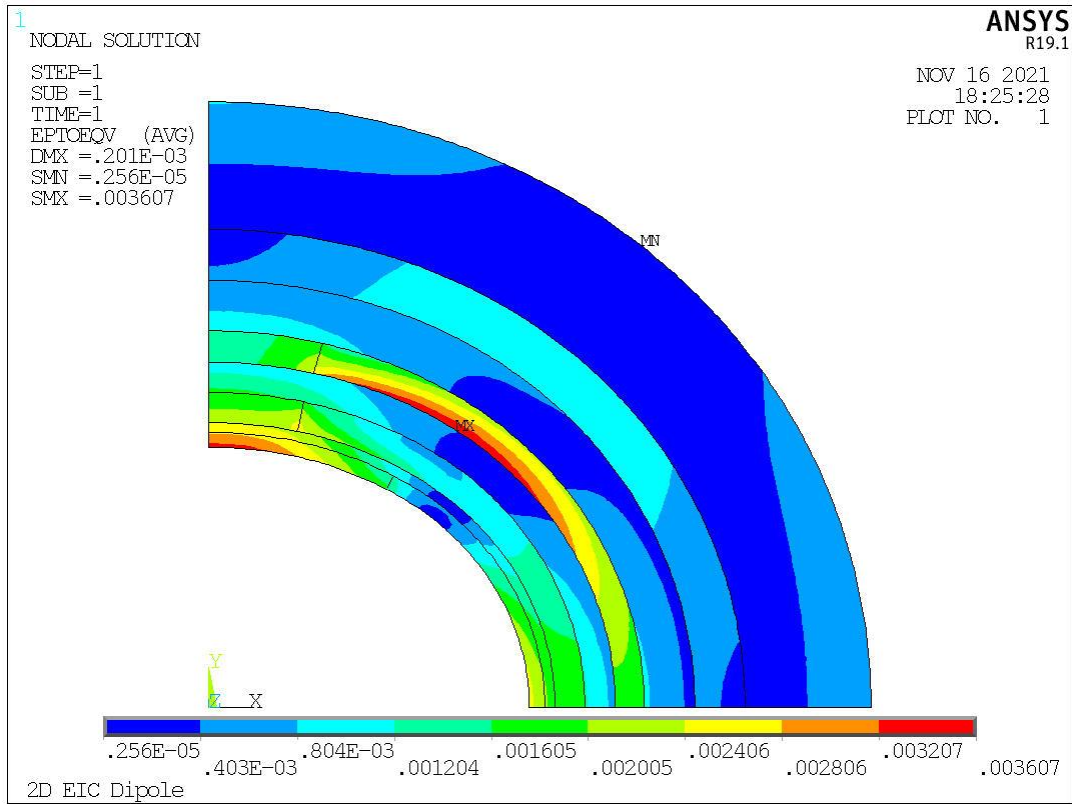


Figure 44: Contour plot of Von Mises strain.

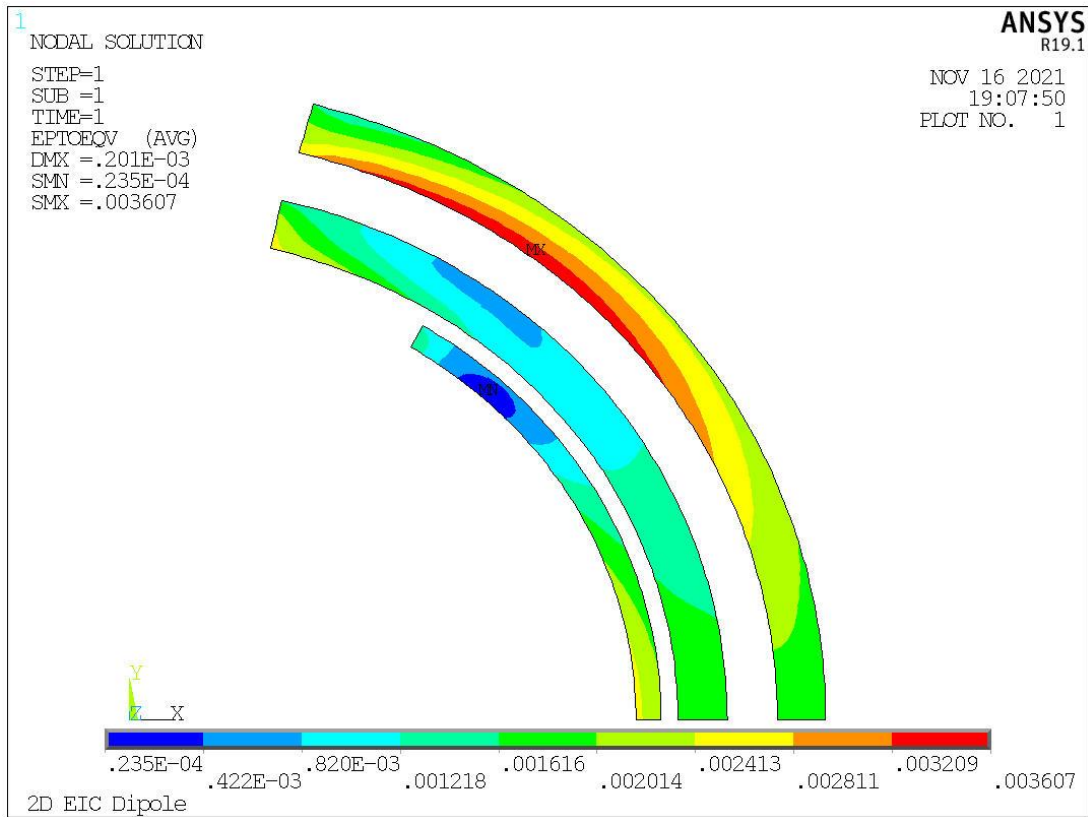


Figure 45: Von Mises strain in the coils.

Case 2: 2-2-6 Configuration

In order to reduce the strain on the coils the layer configuration is varied. In addition, the thickness of the support tubes can be varied. As an example, the two inner super layers each have two layers and the out super layer has been changed to six layers. This keeps the total number of turns the same. Also, the thickness of the inner stainless steel support tube has been increased. Figure 46 shows the displacements for this case. The maximum displacement for this case is now 140  $\mu\text{m}$  which is two thirds of the previous case with a greater reduction near the pole. Figure 47 shows the Von Mises equivalent stress with the peak stress located in the inner support tube. Figure 48 shows the corresponding Von Mises strain which shows a peak strain of 0.35% in the outer super-layer.

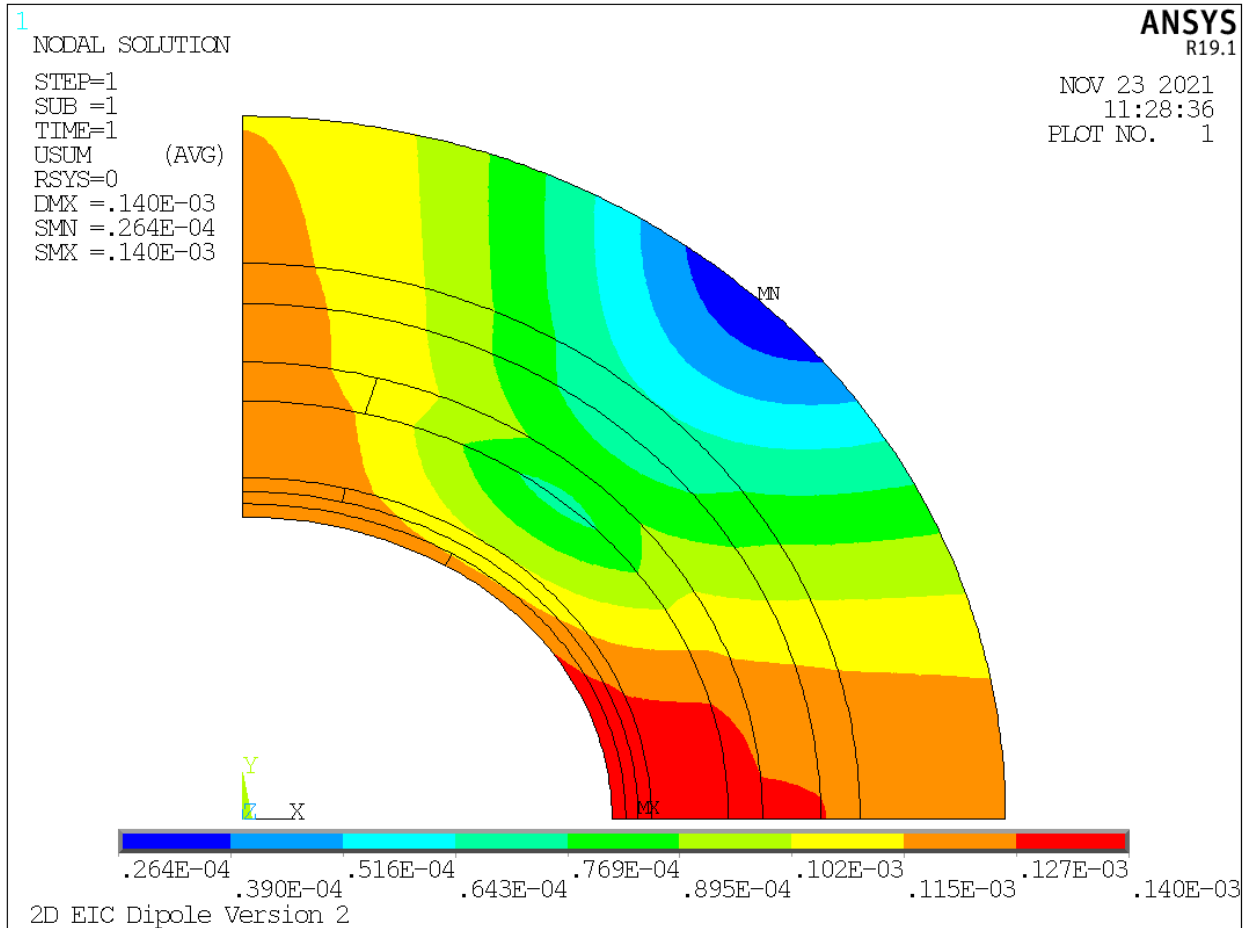


Figure 46: Contour plot of displacements for case 2.

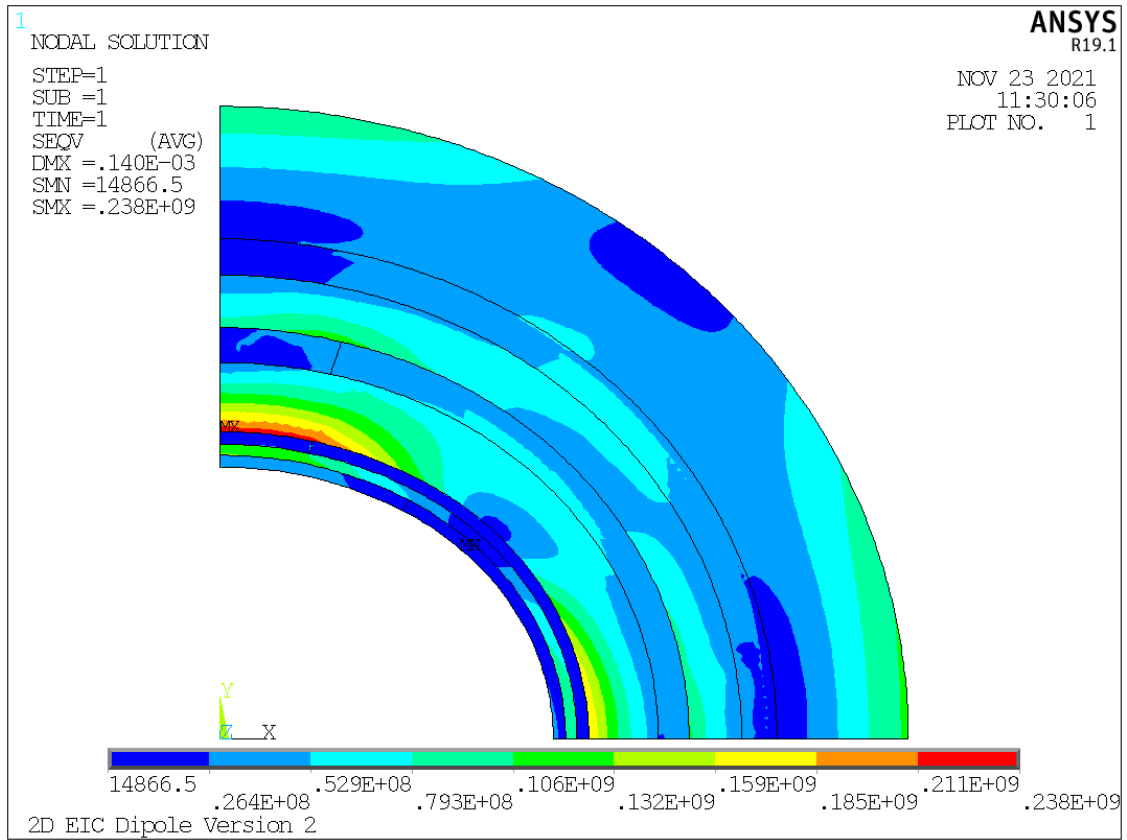


Figure 47: Contour plot of Von Mises stress for case 2

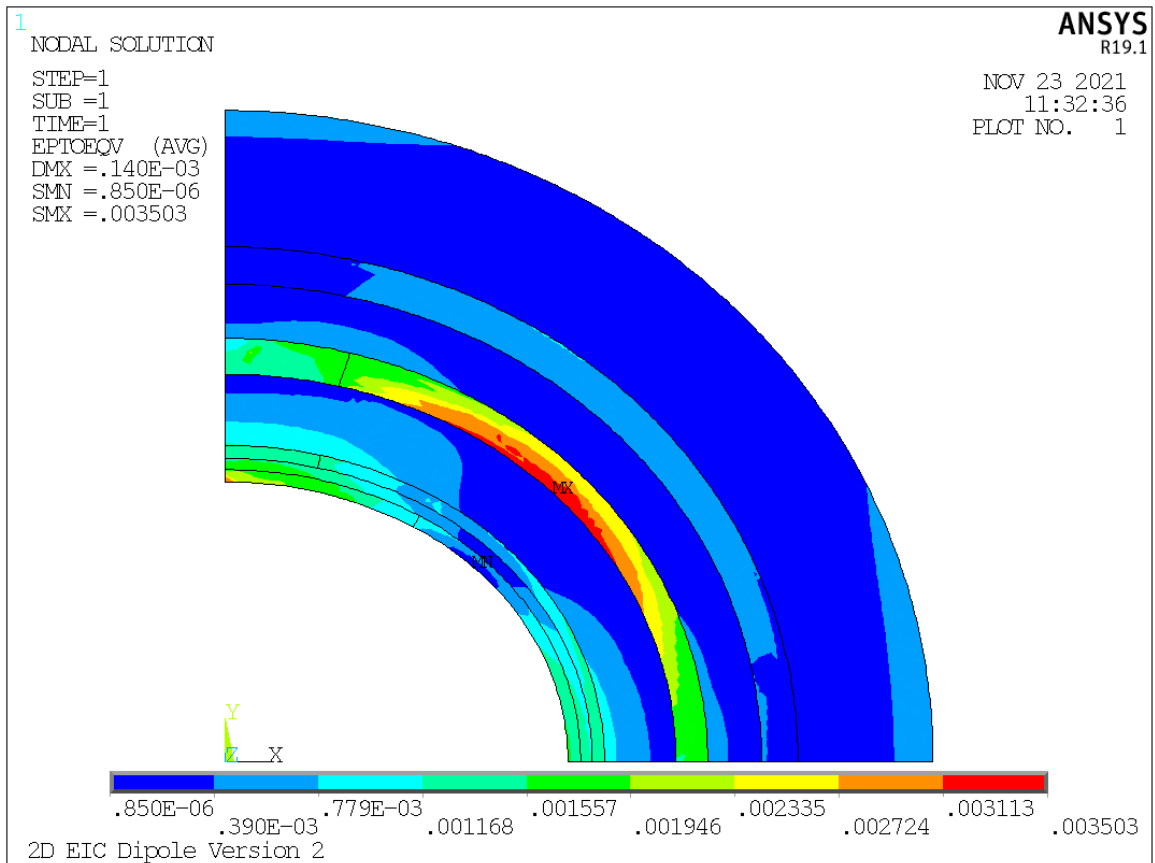


Figure 48: Contour plot of Von Mises strain for case 2

| Case                     | 1        | 2        | 2a       | 2b       | 2c       |
|--------------------------|----------|----------|----------|----------|----------|
| Configuration            | 2_4_4    | 2_2_6    | 2_2_6    | 2_2_6    | 2_2_6    |
| Support #1               | 6 mm     | 13 mm    | 10 mm    | 10 mm    | 20 mm    |
| Support #2               | 10 mm    | 10 mm    | 10 mm    | 15 mm    | 27 mm    |
| Max Displacement         | 201 μm   | 74.0 μm  | 85.5 μm  | 72.1 μm  | 59.9 μm  |
| Von Mises $\sigma_{Eqv}$ | 328 MPa  | 160 MPa  | 162 MPa  | 160 MPa  | 128 MPa  |
| Von Mises strain         | 0.36%    | 0.40%    | 0.40%    | 0.41%    | 0.41%    |
| Coil Displacement        | 201 μm   | 74.0 μm  | 85.5 μm  | 72.1 μm  | 59.9 μm  |
| Coil VM stress           | 63.1 MPa | 69.3 MPa | 69.5 MPa | 72.3 MPa | 71.7 MPa |
| Coil VM strain           | 0.36%    | 0.40%    | 0.40%    | 0.41%    | 0.41%    |

Table 8: Parameters and variables of cases examined.

Table 8 displays the parameters and results of several of the cases examined.

**Case 3: Pre-Tensioning**

After each conductor layer the coil is wrapped in a layer of fiberglass that is applied under tension. This tension can be chosen to apply partial support against the Lorentz forces. This tension can be represented as a radial pressure on the outer surface of the coil by using the equation:  $w\sigma = Pr$  where  $\sigma$  is the tension stress,  $w$  is the layer thickness,  $r$  is the radial distance, and  $P$  is the radial pressure. The integrated forces over the coils are available from Opera. The horizontal forces on the coils are 322 N/mm, -412.4 N/mm, and 243 N/mm respectively for the coils arranged by increasing radius. These forces are spread over the vertical extent of the coils. The pressure is the total horizontal force divided by the vertical extent of the coils. The two inner coils approximately cancel. In this analysis the tension is applied to the outer layer coils.

The radial component of the Lorentz force (from Opera) is expected to look as in Figure 49 with the largest value at the mid-plane and following off at the pole. Tensile stress on the fiberglass sheet would supply a uniform radial force. As the shape of the Lorentz force and tensile radial force are not similar, the tensile force can't fully compensate the Lorentz force at all angles.

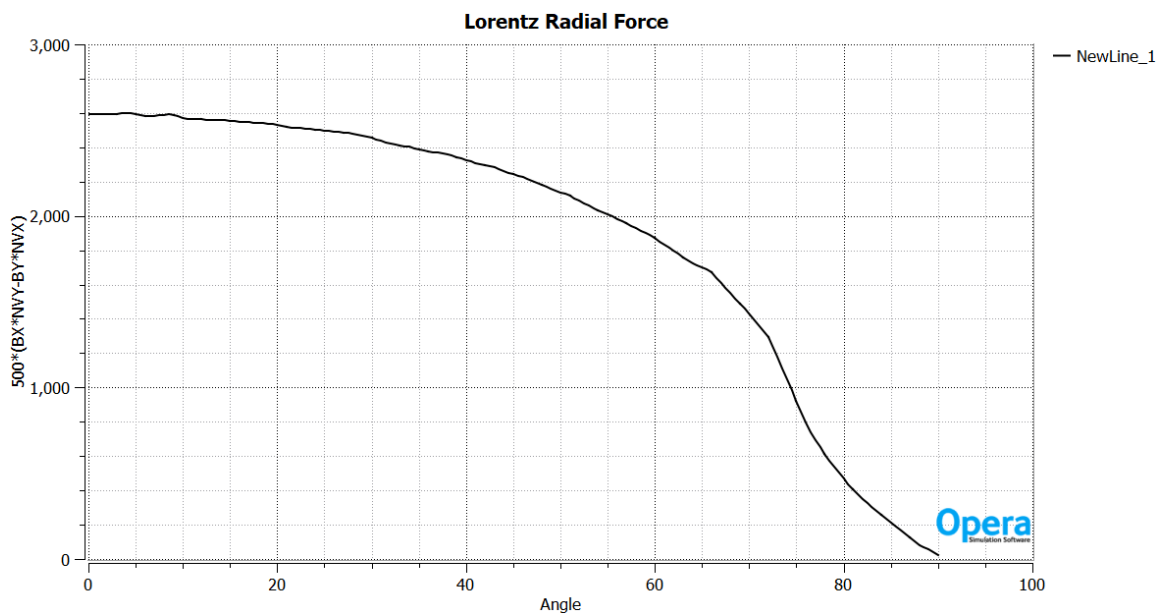


Figure 49: The expected Lorentz radial force calculated at the outer coil in Opera.

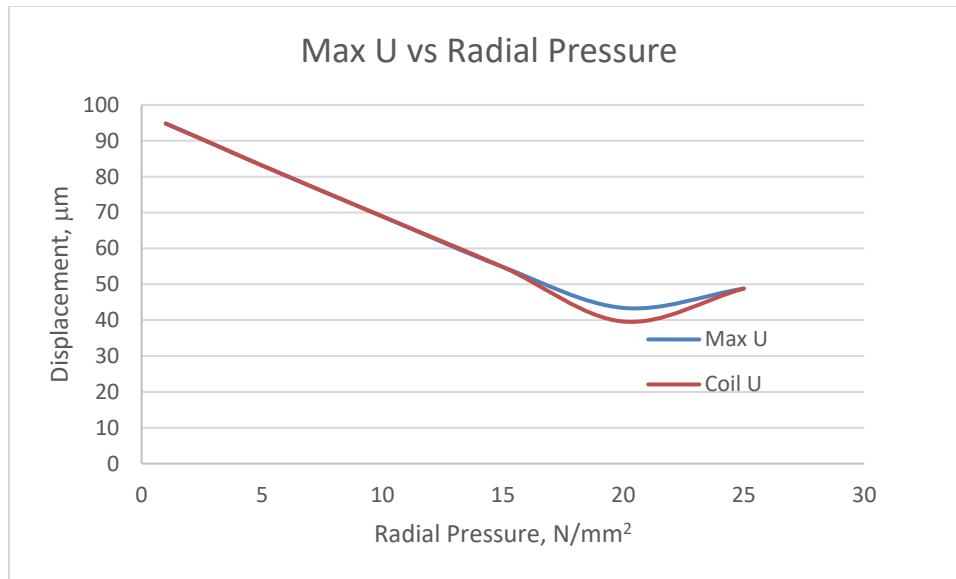


Figure 50: Maximum displacement as a function of applied radial pressure.

Figure 50 shows the maximum displacement as a function of applied radial pressure, P. The red curve shows the maximum displacement in the coils and the blue curve shows the maximum displacement anywhere. The maximum displacement is generally in the coils however it will move away from the midplane with larger radial pressure. As the radial pressure becomes larger the maximum displacement moves from the coils to the stainless-steel support. The tensile stress is  $17.498 \times P$ . The tensile force per mm is  $2.2222 \times P$ . For the radial pressure to match the Lorentz force at the mid-plane, the pressure should be approximately 3 n/mm<sup>2</sup> to 5 n/mm<sup>2</sup>. Figure 51 shows the displacements at P=1 N/mm<sup>2</sup> and at P=25 N/mm<sup>2</sup>. The maximum displacements are near the pole where the Lorentz force is not well matched to the radial tensile force and at the mid-plane where the Lorentz forces are large. As the tension increases the maximum displacement moves to the center.

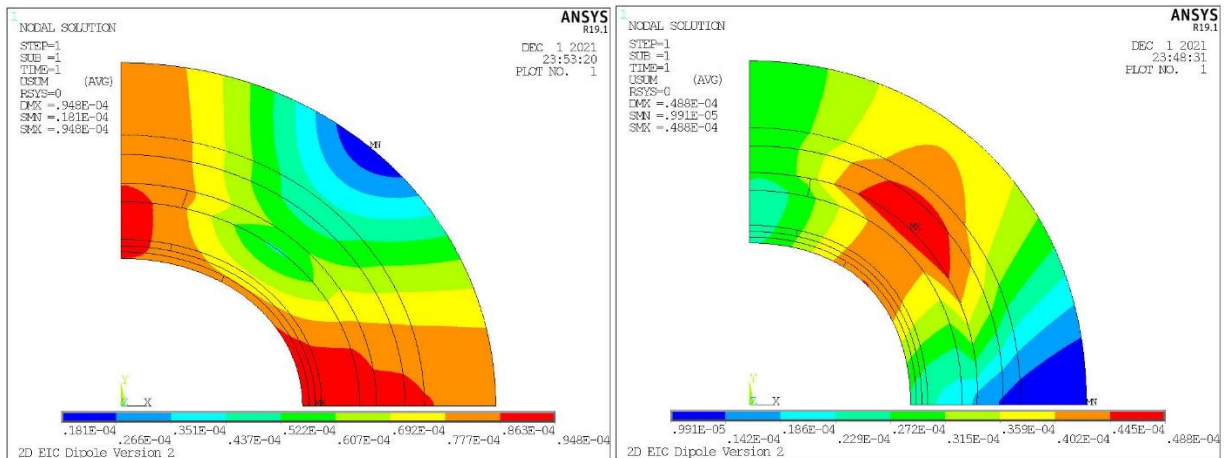


Figure 51: Plot of displacements in meters for radial pressure, P = 1 N/mm<sup>2</sup> (left) and P=25 N/mm<sup>2</sup> (right).

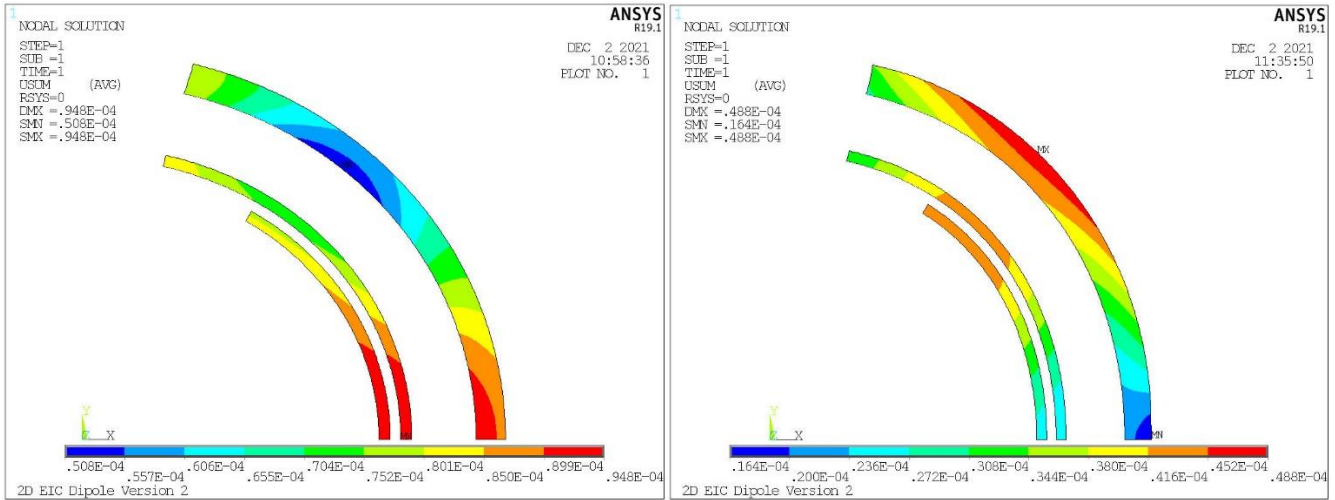


Figure 52: Displacements in the coils in meters for  $P = 1 \text{ N/mm}^2$  (left) and  $P = 25 \text{ N/mm}^2$  (right)

Figure 52 shows the displacements in the coils for radial pressures at  $P = 1 \text{ N/mm}^2$  and  $P = 25 \text{ N/mm}^2$ . This clearly shows that as the tension is increased the maximum displacement in coils moves away from the mid-plane.

The maximum von Mises stress ( $\sigma_{EQV}$ ) as a function of applied radial pressure is shown in Figure 53. The blue curve shows the maximum  $\sigma_{EQV}$  anywhere in the magnet while the red curve shows it in the coils. Since the strain is likely to be similar for the coils and the stainless steel (SS) and the modulus of the SS is larger, the blue curve shows the  $\sigma_{EQV}$  in the SS. The  $\sigma_{EQV}$  varies with a nonlinear function of radial pressure or tensile stress. Figure 54 shows a contour plot of the von Mises stress when  $P = 3 \text{ N/mm}^2$ . The maximum stress is located at the in the SS support adjacent to the outer coil near the mid-plane. As the radial pressure is increased the von Mises stress distribution scales

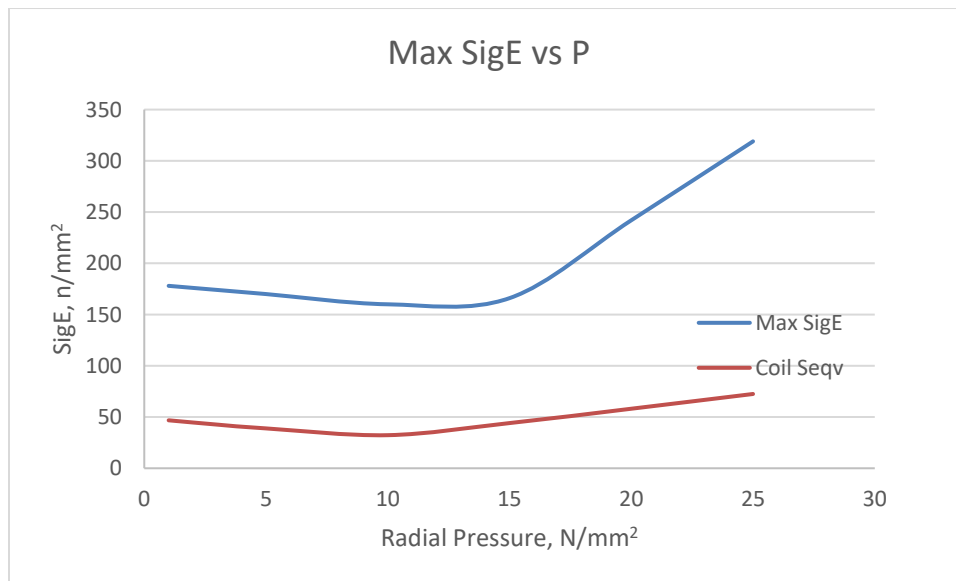


Figure 53: Maximum von Mises stress vs. radial pressure.

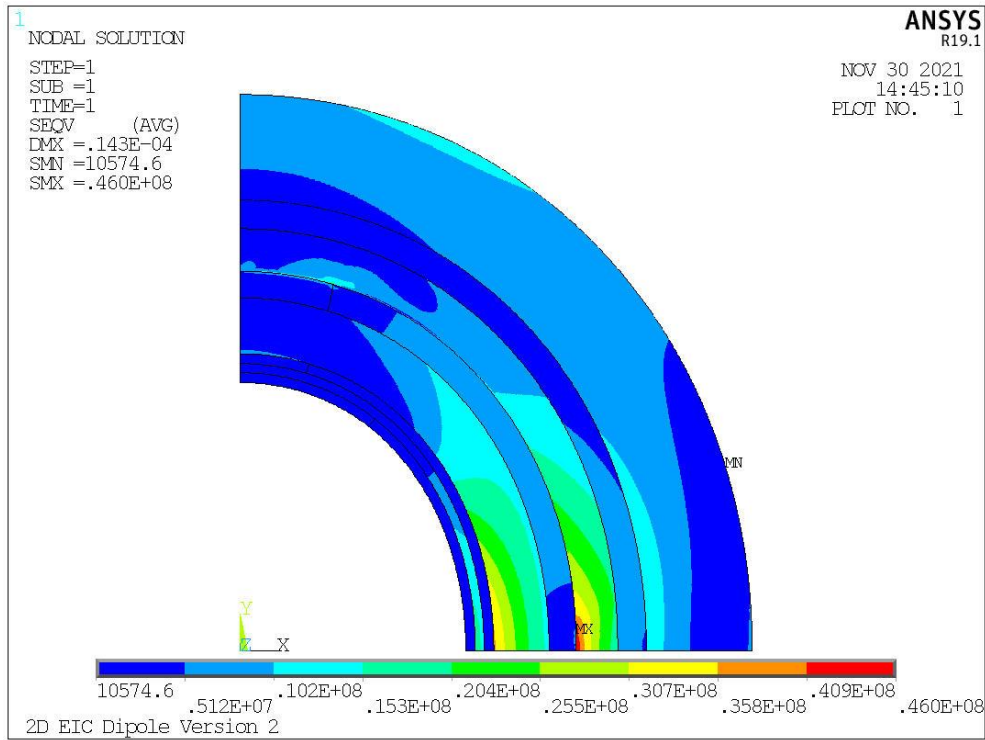


Figure 54: Contour plot of the von Mises stress with radial pressure of 3 n/mm<sup>2</sup>.

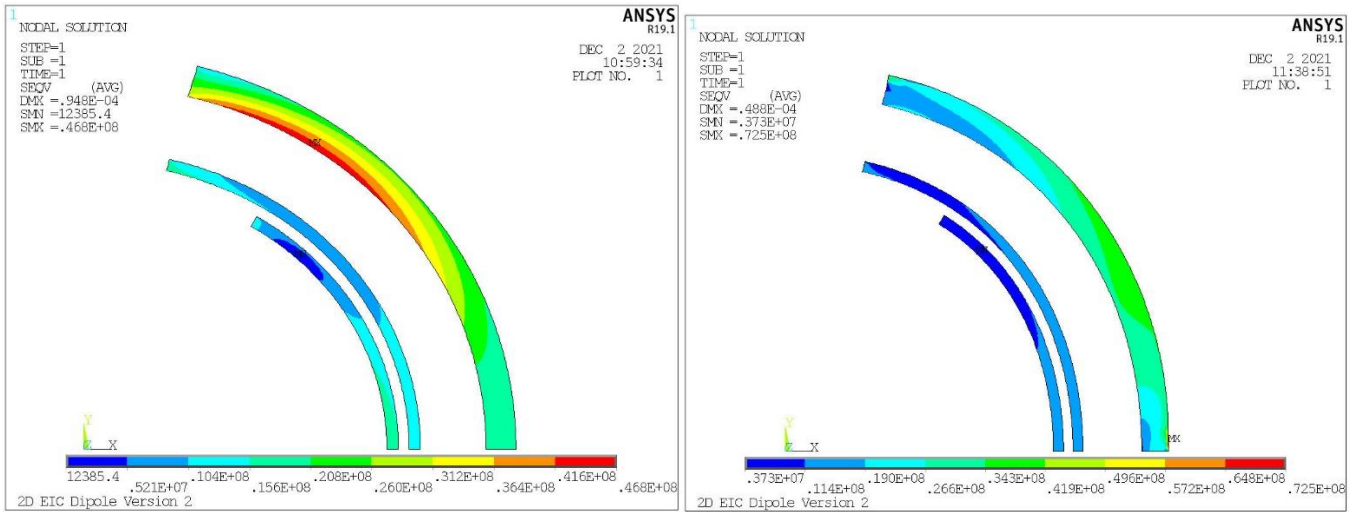


Figure 55: Von Mises stress distribution in the coils for P = 1 N/mm<sup>2</sup> (left) and P = 25 N/mm<sup>2</sup> (right)

Figure 55 shows the  $\sigma_{EQV}$  in the coil for  $P = 1 \text{ N/mm}^2$  and  $P = 25 \text{ N/mm}^2$ . The maximum stress moves toward the mid-plane as the radial pressure increases.

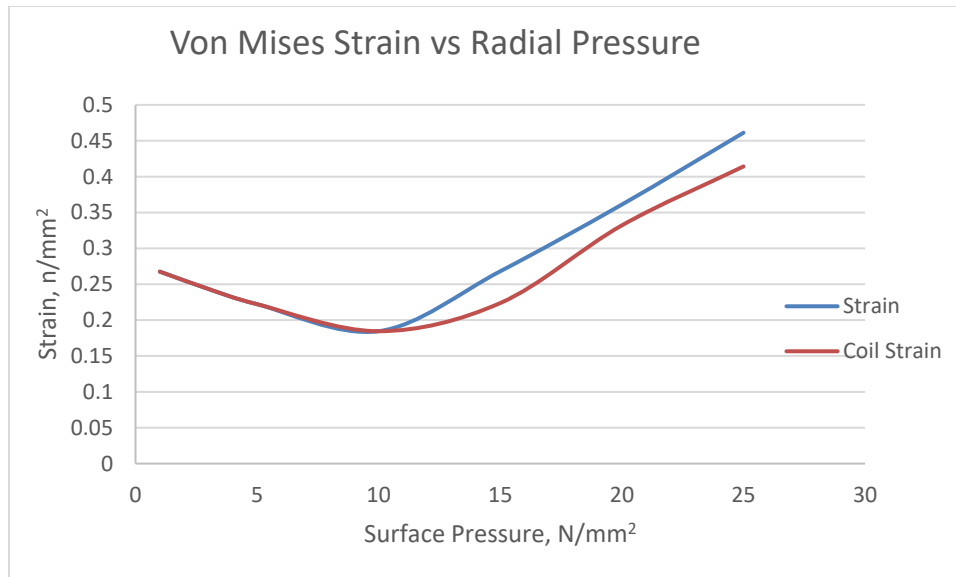


Figure 56: Maximum von Mises strain as a function of radial pressure.

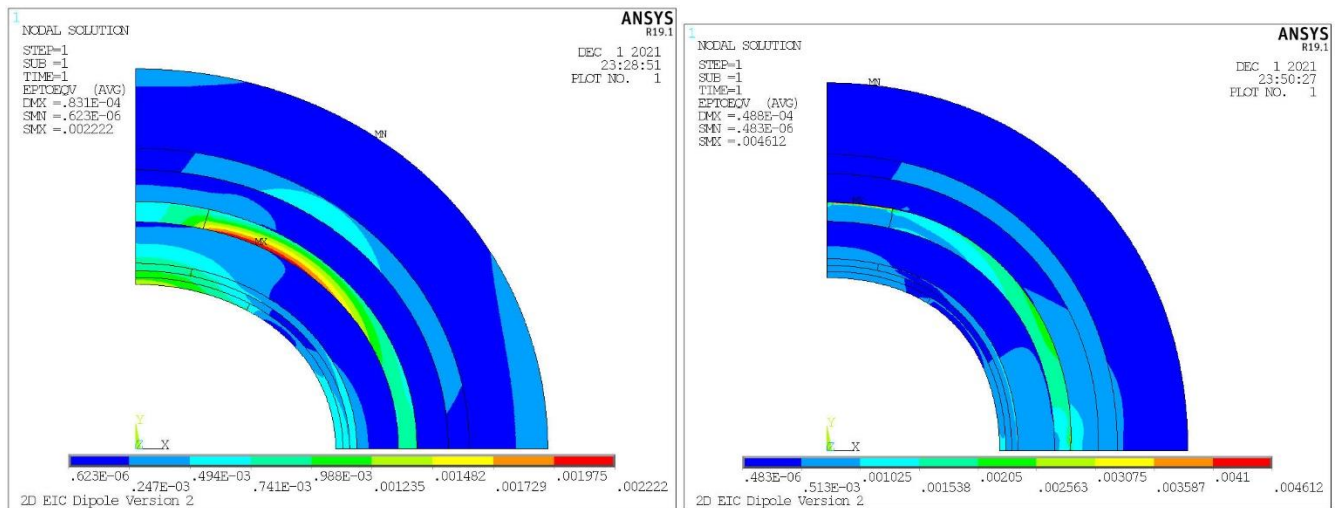


Figure 57: Contour Plot of the von Mises strain at  $P = 5 \text{ N/mm}^2$  (left) and  $P = 25 \text{ N/mm}^2$  (right).

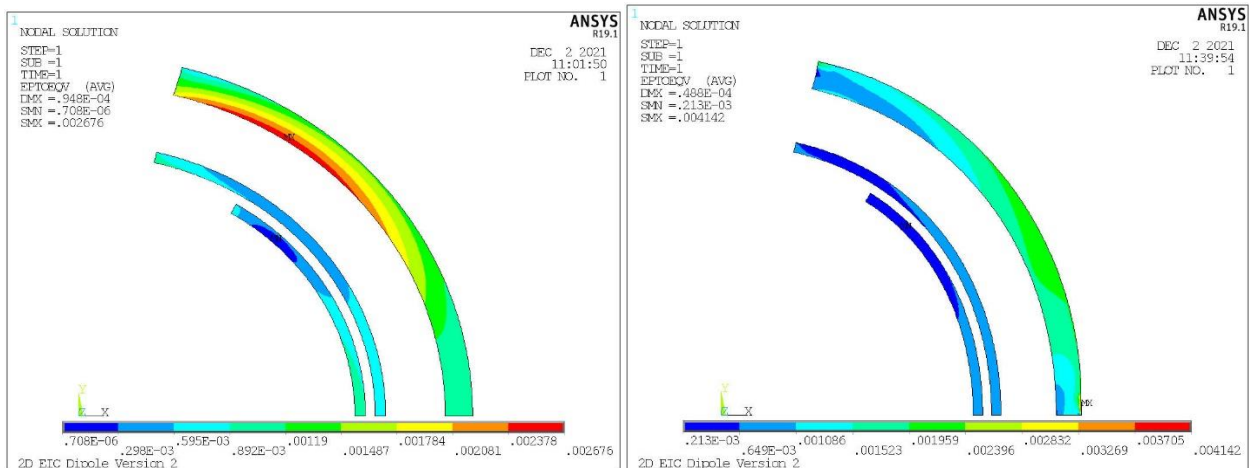


Figure 58: Contour plot of the von Mises strain in the coils at  $P = 1 \text{ N/mm}^2$  (right) and  $P = 25 \text{ N/mm}^2$  (left).

In a similar manner the von Mises strain grows in a nonlinear manner as a function of applied pressure as is shown in Figure 56. The curve in red shows the maximum strain in the coils and the curve in blue shows it in the magnet as a whole. At lower pressure the maximum strain is in the coils. At higher pressures the maximum strain moves off the coils to the adjacent SS support. Figure 57 shows the von Mises strain contour plots for  $P = 5 \text{ N/mm}^2$  and  $P = 25 \text{ N/mm}^2$ , respectively. Also shown in Figure 58 is the von Mises strain in the coils for  $P = 1 \text{ N/mm}^2$  and  $P = 25 \text{ N/mm}^2$ , respectively. The strain pattern varies with the applied tension.

## 4 SUMMARY

The optimum integral design is an efficient design. The relative benefits of it are enormous in short magnets where, for example, length is comparable to coil aperture and still large when the length is a factor of five or so of the coil aperture. The benefit of the optimum integral design for EIC IR dipole B0ApF are clear from Fig. 58 when it is compared with the present design of the same magnet where it creates about 9% higher integral field for the same length by extending the effective magnetic length of the dipole.

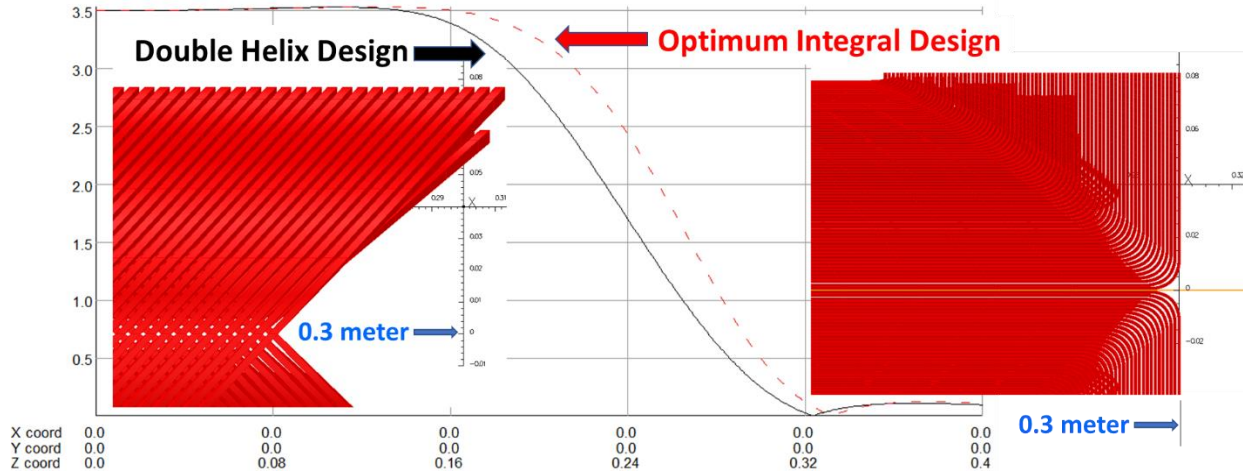


Figure 58: A comparison between the present design and the optimum design for B0ApF when the field is plotted along the axis from the magnet center. The optimum integral design increases the field integral by about 9%.

During the course of Phase I work, we 1) ported the program to design the optimum integral coil; 2) optimized the designs of proof-of-principle Phase I magnet; 3) developed the initial design of the Phase II magnet; and 4) built and tested the proof-of-principle 1.7 T, 114 mm aperture dipole which reached the short sample ion one quench.

The strong outcome and experience gained during Phase I puts us on a strong footing for a promising Phase II proposal.

## 5 REFERENCES

---

1. Nuclear Science Advisory Committee (NSAC) is an advisory committee that provides official advice to the Department of Energy (DOE) and the National Science Foundation (NSF) on the national program for basic nuclear science research. <https://science.energy.gov/np/nsac/>
2. 2015 NSAC Long Range Plan "Reaching for the Horizon", October 20, 2015. [https://science.energy.gov/~media/np/nsac/pdf/2015LRP/2015\\_LRPNS\\_091815.pdf](https://science.energy.gov/~media/np/nsac/pdf/2015LRP/2015_LRPNS_091815.pdf)
3. <https://www.energy.gov/articles/us-department-energy-selects-brookhaven-national-laboratory-host-major-new-nuclear-physics>
4. The Electron-Ion Collider <https://www.bnl.gov/eic/>
5. <https://www.jlab.org/jefferson-lab-be-major-partner-electron-ion-collider-project>
6. EIC Conceptual Design Report: [https://www.bnl.gov/ec/files/eic\\_cdr\\_final.pdf](https://www.bnl.gov/ec/files/eic_cdr_final.pdf)
7. B. Parker et al., "BNL Direct Wind Superconducting Magnets," in IEEE Transactions on Applied Superconductivity, vol. 22, no. 3, pp. 4101604-4101604, June 2012, Art no. 4101604, doi: 10.1109/TASC.2011.2175693.
8. <http://amlsuperconductivity.com/>
9. S. A. Kahn, R. C. Gupta, A. K. Jain, G. H. Morgan and P. A. Thompson, "Calculations of magnetic field for the end design of the RHIC arc dipole," Proceedings of International Conference on Particle Accelerators, 1993, pp. 2754-2756 vol.4, doi: 10.1109/PAC.1993.309450.
10. B. Parker, "The Serpentine Coil Design for BEPC-II Superconducting IR Magnets, presented at the "Mini-Workshop on BEPC-II IR Design", January 12 - 16, 2004, Beijing, P.R. China.
11. H. Witte, B. Parker and R. Palmer, "Design of a Tapered Final Focusing Magnet for eRHIC," in IEEE Transactions on Applied Superconductivity, vol. 29, no. 5, pp. 1-5, Aug. 2019, Art no. 4004105, doi: 10.1109/TASC.2019.2902982.
12. R. Gupta, "Optimum Integral design for maximizing the field in short magnets," in IEEE Trans. on Applied Supercond., vol. 15, no. 2, pp. 1152-1155, June 2005, doi: 10.1109/TASC.2005.849517.
13. <https://root.cern.ch/doc/master/index.html>
14. <http://www.cygwin.com>